Nanoscale

PAPER

View Article Online
View Journal | View Issue

Cite this: *Nanoscale*, 2018, **10**, 8859

The influence of surface functionalization on thermal transport and thermoelectric properties of MXene monolayers†

Sevil Sarikurt, *[a] Deniz Çakır, *[b] Murat Keçeli *[c] and Cem Sevik *[d]

Received 8th December 2017,
Accepted 5th April 2018

DOI: 10.1039/c7nr09144c

rsc.li/nanoscale

The newest members of a two-dimensional material family, involving transition metal carbides and nitrides (called MXenes), have garnered increasing attention due to their tunable electronic and thermal properties depending on the chemical composition and functionalization. This flexibility can be exploited to fabricate efficient electrochemical energy storage (batteries) and energy conversion (thermoelectric) devices. In this study, we calculated the Seebeck coefficients and lattice thermal conductivity values of oxygen terminated M_2CO_2 (where M = Ti, Zr, Hf, Sc) monolayer MXene crystals in two different functionalization configurations (model-II (MD-II) and model-III (MD-III)), using density functional theory and Boltzmann transport theory. We estimated the thermoelectric figure-of-merit, zT, of these materials by two different approaches, as well. First of all, we found that the structural model (*i.e.* adsorption site of oxygen atom on the surface of MXene) has a paramount impact on the electronic and thermoelectric properties of MXene crystals, which can be exploited to engineer the thermoelectric properties of these materials. The lattice thermal conductivity κ_l, Seebeck coefficient and zT values may vary by 40% depending on the structural model. The MD-III configuration always has the larger band gap, Seebeck coefficient and zT, and smaller κ_l as compared to the MD-II structure due to a larger band gap, highly flat valence band and reduced crystal symmetry in the former. The MD-III configuration of Ti_2CO_2 and Zr_2CO_2 has the lowest κ_l as compared to the same configuration of Hf_2CO_2 and Sc_2CO_2. Among all the considered structures, the MD-II configuration of Hf_2CO_2 has the highest κ_l, and Ti_2CO_2 and Zr_2CO_2 in the MD-III configuration have the lowest κ_l. For instance, while the band gap of the MD-II configuration of Ti_2CO_2 is 0.26 eV, it becomes 0.69 eV in MD-III. The zT_{max} value may reach up to 1.1 depending on the structural model of MXene.

1. Introduction

The demonstration of peculiar electronic properties of graphene by Novoselov and co-workers[1] has led researchers to be intensively interested in other 2D materials such as hexagonal boron nitride (h-BN), transition metal dichalcogenides (TMDs), metal oxides and more recently MXenes. MXenes are generally fabricated by chemically etching out A layers from MAX phases, which belong to a family of layered transition metal carbides and metal nitrides. The chemical formula of the MAX phase is given by $M_{n+1}AX_n$ (n = 1, 2, 3), where M is an early transition metal, A is mainly an element from group IIIA or IVA and X is C and/or N.[2] After etching the A layer, the surface of each MXene layer is terminated by surface groups such as F, H, OH and/or O due to the chemical fabrication process. The final functionalized MXene structures are given by the formula $M_{n+1}X_nT_{n+1}$ (T = F, H, OH, O).

Various experimental studies demonstrated that MXene crystals have extensive and growing application areas. Up to now, Ti_3C_2,[3] Ti_2C, Ta_4C_3, TiNbC, $(V_{0.5}, Cr_{0.5})_3C_2$, Ti_3CN,[2] Nb_2C, V_2C,[4] Nb_4C_3,[5] Mo_2C,[6] Mo_2TiC_3[7] and Ti_4N_3[8] layered MXene structures have been synthesized experimentally and some of these materials have been already proposed for different technological applications such as Li-ion batteries,[9–12] supercapacitors,[13–15] fuel-cells,[16] hydrogen storage[17,18] and electronic devices.[19,20] Furthermore, experimental results on temperature dependent thermoelectric (TE) properties of freestanding MXene materials (Mo_2CT_x, $Mo_2TiC_2T_x$, $Mo_2Ti_2C_3T_x$) have

[a]Department of Physics, Faculty of Science, Dokuz Eylul University, Izmir, 35390, Turkey. E-mail: sevil.sarikurt@deu.edu.tr
[b]Department of Physics and Astrophysics, University of North Dakota, Grand Forks, North Dakota 58202, USA. E-mail: deniz.cakir@und.edu
[c]Chemical Sciences and Engineering Division, Argonne National Laboratory, Argonne, Illinois 60439, USA. E-mail: keceli@anl.gov
[d]Department of Mechanical Engineering, Faculty of Engineering, Anadolu University, Eskisehir, 26555, Turkey. E-mail: csevik@anadolu.edu.tr.

†Electronic supplementary information (ESI) available. See DOI: 10.1039/C7NR09144C

been reported recently.[21] The measurements showed that the Mo-based MXenes have high electrical conductivity and relatively large Seebeck coefficient values that lead to a better TE performance of these materials than their parent ternary and quaternary layered carbides. Additionally, authors also proposed, based on their overall results, that this promising performance can further be enhanced by additional doping, controlling the surface functional groups, and/or hybridization with semiconductor materials or polymers.

Also, the electronic properties and the dynamic stability of some MXene structures have been investigated theoretically by different research groups. The thermoelectric properties of functionalized M_2C (M = Sc, Ti, V, Cr, Zr, Nb, Ta) and M_2N (M = Ti, Cr, Zr) structures with F, OH and O have been analyzed by Khazaei *et al.*[22] They considered four different functionalization models, Model I (MD-I)–Model IV (MD-IV), and obtained the most energetically stable ones. They have reported that Ti_2CO_2, Hf_2CO_2, Zr_2CO_2, and Sc_2CT_2 (T = F, OH, O) MXene structures exhibit semiconductor behaviour with a small band gap of 0.24, 1.0, 0.88, 1.03, 0.45 and 1.8 eV, respectively. Their results suggested that Ti_2CO_2 would be a good candidate for TE device applications. The structural, mechanical and electronic properties of M_2CT_2 (M = Sc, Ti, V, Cr, Zr, Nb, Mo, Hf, Ta, W) MXene structures have been investigated by Zha *et al.*[23] They have shown that the transition metal atom and the surface functional groups (T = F, OH, O) have a considerable influence on the crystal structure of these materials and the oxygen functionalized MXene structures possessing smaller lattice parameters show superior mechanical stability as compared to fluorine and hydroxyl functionalized ones. In addition to the structural properties, the influence of the functionalization also on the electronic and thermal properties of MXene structures has been reported in several other studies.[24–26] Zha *et al.* have also investigated the electronic and thermal properties of Sc_2CT_2 (T = F, OH),[27] Hf_2CO_2, Ti_2CO_2, and Zr_2CO_2[28] MXene crystals. They have found that $Sc_2C(OH)_2$ is the only semiconductor with an intrinsic direct band gap among all the Sc based MXene crystals that they have studied. Also, they have determined that the lattice thermal conductivity κ_l value increases with increasing atomic number of transition metals that they considered and showed that Ti_2CO_2 might be a better candidate for nanoelectronic applications due its high electron mobility and also low κ_l. Furthermore, Gandi *et al.*[29] have performed calculations for the TE properties of M_2CO_2 (M = Ti, Zr, Hf) MXene structures and they have demonstrated that the band gap grows with increasing mass of the transition metal and the Ti_2CO_2 crystal has the best TE performance due to its lower κ_l. Yorulmaz *et al.*[30] have investigated the dynamic and mechanical stability of 80 functionalized M_2XT_2 (M = Sc, Mo, Ti, Zr, Hf; X = C, N; T = O, F) MXene structures systematically and reported the most energetically favorable models for each MXene system. They have found that MD-II and MD-III configurations of M_2CO_2 (M = Ti, Zr, Hf), MD-III configuration of Sc_2CO_2 and M_2CF_2 (M = Sc, Zr, Hf) and also MD-II and MD-IV configurations of Sc_2CF_2 MXene monolayers demonstrate semiconductor characteristics and stable dynamical properties. In summary, the recently reported experimental measurements and previous theoretical studies have clearly pointed out that the thermoelectric properties of MXene crystals are needed to be further examined, particularly taking into account surface effects.

Thermoelectric materials (TEMs) are mainly used for refrigeration and power generation through the conversion of a temperature gradient into electricity, or *vice versa*. Flexible in size and shape and without any mechanical parts, TE devices offer unique advantages compared to conventional refrigerators and generators. However, their usage is still limited due to their lower TE efficiency, which can be evaluated *via* a dimensionless TE figure-of-merit defined as $zT = S^2\sigma T/\kappa$, where S is the Seebeck coefficient (or thermopower), σ is the electrical conductivity, T is the temperature and κ is the total thermal conductivity that includes contributions from the lattice (phonon) thermal conductivity (κ_l) and the electronic thermal conductivity (κ_e). A good TE material should display a "high" power factor, $S^2\sigma$, and "low" thermal conductivity, κ, but this elusive target has challenged researchers for decades. As mentioned above, the functionalized MXene materials have prominent electronic, mechanical and thermal properties[22,27–30] and thus it is imperative to study their electronic and thermal transport properties in order to estimate their potential as thermoelectric materials.

In this respect, we have calculated the electronic and thermal transport properties of M_2CO_2 (M = Ti, Zr, Hf, Sc) monolayer MXene crystals by utilizing first principles electronic structure calculations and solving the linearized Boltzmann transport equation (BTE)[31–33] for both electrons and phonons. Our results provide qualitative and quantitative information on the importance of the chemical composition and structural configuration of different MXenes and guidance to experimental studies for materials with higher TE efficiency.

2. Computational methods

The electronic and thermal properties of all the considered systems were predicted by first-principles calculations based on density functional-theory (DFT) and density-functional perturbation theory (DFPT), as implemented in the Vienna *ab initio* simulation package (VASP) code.[34,35] The exchange–correlation interactions were treated using the generalized gradient approximation (GGA) within the Perdew–Burke–Ernzerhof (PBE) formulation[36] and the single electron wave functions were expanded in plane waves with a kinetic energy cutoff of 450 eV, for all the simulations. For structure optimizations, the Brillouin-zone integrations were performed using a Γ-centered regular 16 × 16 × 1 k-point mesh within the Monkhorst–Pack scheme.[37] The convergence criteria for electronic and ionic relaxations were set to 10^{-7} eV and 10^{-4} eV Å^{-1}, respectively. A 15 Å vacuum layer along the z-direction was adopted to prevent any interaction between neighboring layers.

Lattice thermal transport properties were determined by the self-consistent solution of the Peierls–Boltzmann transport

equation[38] as implemented in the ShengBTE code.[39] Long-range electrostatic interactions (nonanalytical correction) are included by using the Born effective charges and the dielectric tensor calculated by VASP. The second-order inter-atomic force constants (IFCs) required by the ShengBTE were obtained by the PHONOPY[40] code which extracts the proper force-constant file from the results predicted by DFPT. The third-order IFCs were derived from the VASP calculations of the structures generated by considering up to seven (eight) next-nearest-neighbor interactions for MD-II (MD-III). Here, $4 \times 4 \times 1$ supercell structures and a Γ-centered regular $4 \times 4 \times 1$ k-point mesh were used in the DFT calculations performed to predict the second- and third-order IFCs, respectively. In lattice thermal transport calculations at least a $80 \times 80 \times 1$ well converged q-grid and a 6.00 Å out of plane lattice constant, d, were used for all the considered single layer materials to make a reliable comparison of monolayer structures with each other. The upper limit for the temperature range was set to 700 K to ensure that all MXene structures are solid, since molecular dynamics simulations predicted that Ti_2CO_2 starts melting at 823 K.[41]

The Seebeck coefficient, the electrical conductivity (σ/τ) and the electronic thermal conductivity (κ_e/τ) were calculated by using relaxation time approximation (RTA) as implemented in the BoltzTraP[42] software package based on the Wiedemann–Franz law. Here, a Γ-centered regular $64 \times 64 \times 1$ k-point mesh was adopted to obtain the band energies to be used in BoltzTraP calculations. Although the relaxation time (τ) depends on the electronic wave vector, energy, and scattering mechanism, the RTA has been shown to provide reasonable results for various materials.

3. Results and discussion

In this study, we systematically investigated and compared the thermoelectric potential of seven different semiconductor monolayer MXene structures, M_2CO_2 (M = Ti, Zr, Hf, Sc). Depending on the lattice positions of functional groups (here it is oxygen), we considered two different crystal configurations (MD-II & MD-III), depicted in Fig. 1, for all the monolayers except for Sc_2CO_2, for which only semiconductor structure MD-III was considered.

The crystal symmetries of the MD-II and MD-III structures are $P\bar{3}m1$ and $P3m1$, respectively. Due to the inversion symmetry, both C–metal (and also O–metal) bonds have equal lengths in the MD-II structure. Conversely, due to the absence of such inversion symmetry, we have two different bond lengths for the C–metal and O–metal bonds in the MD-III structure. For instance, while the C–metal (O–metal) bond length is 2.19 Å (1.98 Å) in MD-II of Ti_2CO_2, it becomes 2.22 and 2.16 Å (2.00 and 1.98 Å) in MD-III of Ti_2CO_2. This structural asymmetry brings different stabilities, and electronic, vibrational, thermal and thermoelectric properties in MD-III as compared to MD-II. For instance, lower stabilities and longer bond lengths may result in softer vibrational frequencies in the MD-III structure, thereby leading to reduced thermal conductivity.

The calculated electronic band structures and phonon dispersion curves of all the scrutinized monolayer crystals along the high symmetry directions of the Brillouin zone are given in the ESI.† The group velocity is also indicated by the line color in phonon dispersion curves. Beside these, we demonstrated the total density of states and partial density of states of each atom composing M_2CO_2 MXene structures in the ESI (Fig. S5†). As indicated in Fig. S1–S3† in the ESI, MD-II and MD-III configurations of M_2CO_2 (M = Ti, Zr, Hf) were found to be indirect band semiconductors. Sc_2CO_2-MD-III has the widest indirect band gap of 1.76 eV and the MD-II configuration of Ti_2CO_2 has the smallest band gap with a value of 0.26 eV. In the presence of mixed conduction due to small band gap values, the holes and electrons counteract each other, lowering the power factor. In this respect, the MD-II to MD-III structural transition in Ti_2CO_2 possibly suppresses the bipolar conduction at elevated temperatures, enhancing the Seebeck coefficient. The calculated band gap values of these structures, given in Table 1, are in excellent agreement with the previous calculations.[22,23,30,41,43] The effect of the structural model on the electronic properties is the largest in Ti_2CO_2 and it becomes less effective when moving from Ti to Hf. The band gap difference is 0.40 eV for Ti_2CO_2, 0.14 eV for Zr_2CO_2 and 0.07 eV for Hf_2CO_2, see Table 1. Interestingly, the band gap values increase when going from Ti to Hf in both structural models. Since MD-II of Ti_2CO_2 has the smallest band gap, it is expected that, at high temperatures and low carrier concen-

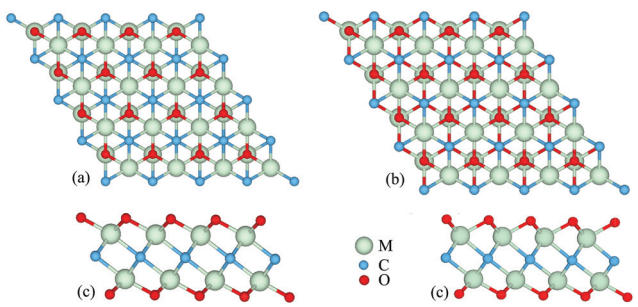

Fig. 1 Schematic illustration of functionalized M_2XT_2 MXene systems: top views of (a) MD-II and (b) MD-III; side views of (c) MD-II and (d) MD-III.

Table 1 Positions of valence band maximum (V_{max}) and conduction band minimum (C_{min}), and the corresponding band gap energies for the MD-II and MD-III configurations of M_2CO_2 (M = Ti, Zr, Hf, Sc)

	MDII			MDIII		
	E_g (eV)	V_{max}	C_{min}	E_g (eV)	V_{max}	C_{min}
Ti_2CO_2	0.26	Γ	M	0.69	Γ–K	Γ–M
Zr_2CO_2	0.91	Γ	M	1.05	Γ–K	Γ–M
Hf_2CO_2	1.02	Γ	M	1.09	Γ	M
Sc_2CO_2	—	—	—	1.76	Γ	K

trations, both electrons and holes contribute to heat transport, and increase the overall thermal conductivity, thereby reducing the Seebeck coefficient and increasing the electrical conductivity. However, the MD-III configuration of Ti_2CO_2 can exhibit enhanced TE properties due to its much larger band gap as compared to its MD-II configuration. As a representative, Fig. 2 shows the band structures and orbital resolved density of states of MD-II and MD-III of Ti_2CO_2. Zr and Hf based MXenes have similar electronic properties. The valence band (VB) edge has the main contribution coming from C-2p orbitals while the M-d orbital mainly contributes to the conduction band (CB) edge in the MD-II structure. The weights of the atomic orbitals significantly change throughout the high symmetry directions in the first Brillouin zone. In MD-III, the p orbital of oxygen atoms moves towards the Fermi level and dominates the valence band edge. Concerning the valence band of the MD-III structure, there are two peaks with almost the same energies (*i.e.* they are all accessible by carrier doping), located at the Γ point and a point close to K along the Γ–K direction. It has been previously shown that such a multi-valley/peak structure in Bi_2Te_3, Sb_2Te_3[44] and SnSe[45] leads to a large TE power factor, $S^2\sigma$. Therefore, in the MD-III structure, the formation of a new extreme located between Γ–K points, which is 1 eV below in the MD-II structure, may be expected to enhance S and thus, $S^2\sigma$. Furthermore, the bands forming the lowest conduction band are very flat in both structural models, whereas the valence band of MD-II has a much larger dispersion (spreading over 3 eV). Such difference in the valence band of the MD-II and MD-III structures gives rise to a larger hole effective mass in the former, thereby leading to a significantly enhanced p-type Seebeck coefficient in the MD-III structure.

The effective mass, m^*, of electrons and holes is also significantly affected from the surface termination model. The conduction band minima of all the MD-II structures and the MD-III structure of Hf_2CO_2 are located at the M point as seen in Fig. 3(a) and (c), whereas the conduction band minima of Ti_2CO_2 and Zr_2CO_2 are close to the M point along the Γ–M direction. For all the materials, the highly anisotropic effective masses are heavier in the MD-III structure in all directions as compared to the MD-II structure. The hole effective masses at the Γ point are around 0.15–0.50 and 0.60–1.10m_0 (where m_0 is the mass of electron in free space) for MD-II and MD-III, respectively, as seen in Fig. 3(d). However, the hole effective mass values corresponding to the newly emerged band in the MD-III structures, where the band extreme is located close to the K point along the Γ–K direction, are significantly anisotropic. This band is very flat along the direction perpendicular to the Γ–K with hole effective masses of ~7.00 for Ti_2CO_2 and

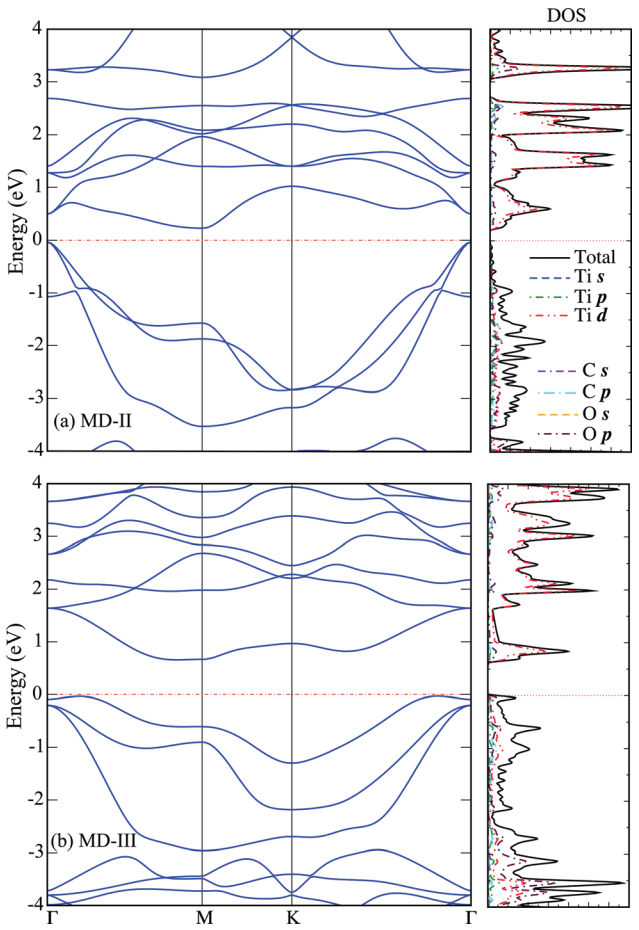

Fig. 2 Band structure and orbital resolved density of states of (a) MD-II and (b) MD-III structures of Ti_2CO_2.

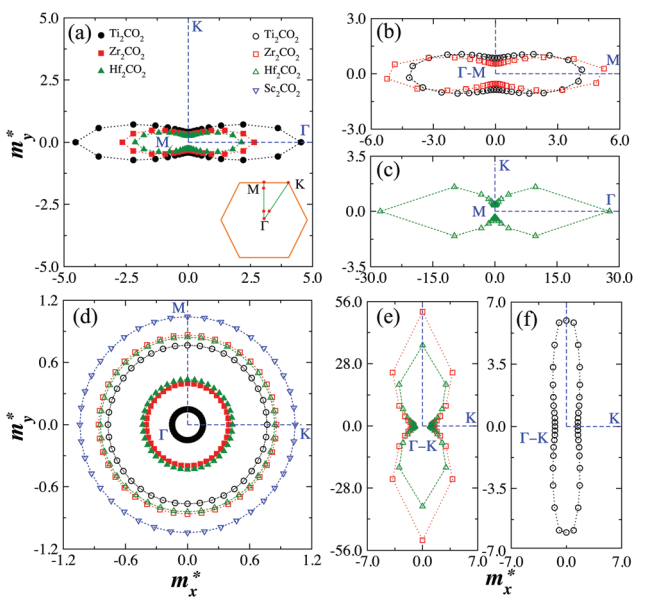

Fig. 3 Direction dependent electron effective masses for (a) Ti, Zr, and Hf based MD-II structures, (b) Ti and Zr based MD-III structures, and (c) Hf based MD-III structure, and hole effective masses for (d) Ti, Zr, Hf, and Sc based MD-II and MD-III structures, (e) Ti and Zr based MD-III structures, and (f) Hf based MD-III structure. Here, Γ, M, K, Γ–M, and Γ–K depict the center of the band extrema and Brillouin zone directions. Each data point represents the end point of a vector whose amplitude corresponds to the effective mass in units of m_0 and the direction of this vector corresponds to the direction (Cartesian coordinates) in the k space along which the mass is calculated.

surprisingly >28.00m_0 for Zr_2CO_2 and Hf_2CO_2, as seen in Fig. 3(e) and (f).

Phonon dispersion curves for all the structures display positive frequencies in the whole Brillouin zone, demonstrating dynamic stability at T = 0 K (Fig. S6–S9 in the ESI†). Since there are 5 atoms in the primitive cell of the M_2CO_2 system, there are 15 vibrational modes: the lowest 3 of them are acoustic modes (known as in-plane longitudinal acoustic mode (LA), transverse acoustic mode (TA) and out-of-plane transverse acoustic (or flexural acoustic) mode (ZA)) and the remaining ones are optical modes. The frequencies of the in-plane LA and TA branches exhibit a linear dispersion around the Γ point whereas the ZA branch has a quadratic dispersion in the long wavelength limit. The vibrational direction of the ZA mode is definitely perpendicular to the monolayer plane as in the other 2D structures like graphene,[46] phosphorene,[47] and stanene.[48] The ZA mode is of great importance in understanding the thermal and mechanical properties of 2D materials.[49–51] The ZA branch is less dispersive in MD-III than in MD-II. In general, the group velocities of phonon modes in MD-III are usually comparable to those in MD-II when we include non-analytical term correction which mostly affects the optical modes. In all structures, there are low frequency optical branches near the acoustic branches enhancing the possibility of Umklapp scattering that involves an acoustic mode and an optical mode.[52] In Hf-based MXenes, the high lying optical modes are well separated from the low lying ones indicating a lower probability of three-phonon scattering between the optical phonons. Hence, Hf-based MXenes have higher κ_l.

In order to find out the TE efficiency of the considered MXene materials, we computed the Seebeck coefficient, electrical conductivity and electronic thermal conductivity with constant RTA. We first estimated the maximum value of the TE figure-of-merit, zT_{max}, with the assumption of vanishing κ_l ($zT_{max} = S^2\sigma T/\kappa_e$). We plotted the absolute values of Seebeck coefficients and also zT_{max} values for both n- and p-type doping as a function of charge carrier density at three different temperatures, namely, T = 300, 500 and 700 K, as shown in Fig. 4–7. The charge carrier densities were calculated by integrating the density of states for both p-type and n-type doping. At a given temperature and charge carrier density, the MD-III configurations exhibit higher Seebeck coefficients and zT_{max} as compared to MD-II configurations. The origin of a high Seebeck coefficient in the MD-III structures can be partially attributed to their more complex band structures and heavier carrier effective masses as discussed above. The influence of the configuration is more specifically observed in Ti_2CO_2, especially at lower carrier densities. Consistent with the fact that the Seebeck coefficient is adversely proportional to the carrier density, we have lower Seebeck coefficients at high doping concentrations. While the n-type Seebeck coefficient is significantly higher than the p-type one in MD-II, we have comparable n and p-type Seebeck coefficients in MD-III, due to the presence of a highly flat valence band in the latter. As seen from Fig. 6(e), the p-type Seebeck coefficient of the MD-III

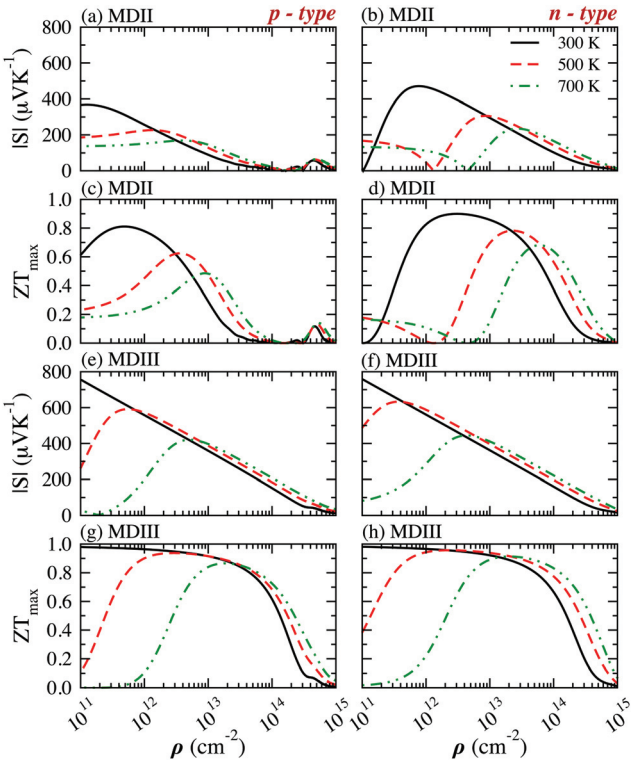

Fig. 4 Seebeck coefficient and maximum TE figure-of-merit as a function of carrier density at T = 300, 500, and 700 K of Ti_2CO_2. Plots for the MD-II and MD-III configurations are represented in a–d and e–h, respectively.

structure of Hf_2CO_2 has a different variation with carrier concentration at T = 300 K. The reason for this behavior can be revealed if one thoroughly inspects the band structure and density of states plots, see the ESI.† In contrast to the MD-III structures of Ti_2CO_2 and Zr_2CO_2, which have large DOS at the top valence band due to the flat band, the DOS corresponding to the top of the valence band is very small in the MD-III structure of Hf_2CO_2. This is due to the fact that the flat band is slightly below the more dispersive bands in the MD-III structure of Hf_2CO_2.

The maximum attainable values for the Seebeck coefficient at room temperature were found to be around 480, 680, and 650 μV K^{-1} for the n-type carrier concentrations in the MD-II configuration of Ti_2CO_2, Zr_2CO_2 and Hf_2CO_2, respectively. Both p-type and n-type carrier concentrations in the MD-III configuration of Ti_2CO_2 and Zr_2CO_2 acquire a Seebeck coefficient of approximately 750 and 800 μV K^{-1} (in respective order). Similarly, for the n-type doping of Hf_2CO_2 in the MD-III configuration the maximum Seebeck coefficient was estimated as approximately 700 μV K^{-1}. Furthermore, the Seebeck coefficient of the p-type and n-type in the MD-III structure of Sc_2CO_2 has an approximate value of about 600 μV K^{-1}. These calculated Seebeck coefficient values are comparable to, even better than, those of the well-known TE material $SrTiO_3$, Bi_2Te_3 nanowires, and Te/Bi_2Te_3 nanowire heterostructure composites, exhibiting a Seebeck coefficient of 850 μV K^{-1} at around 90 K,

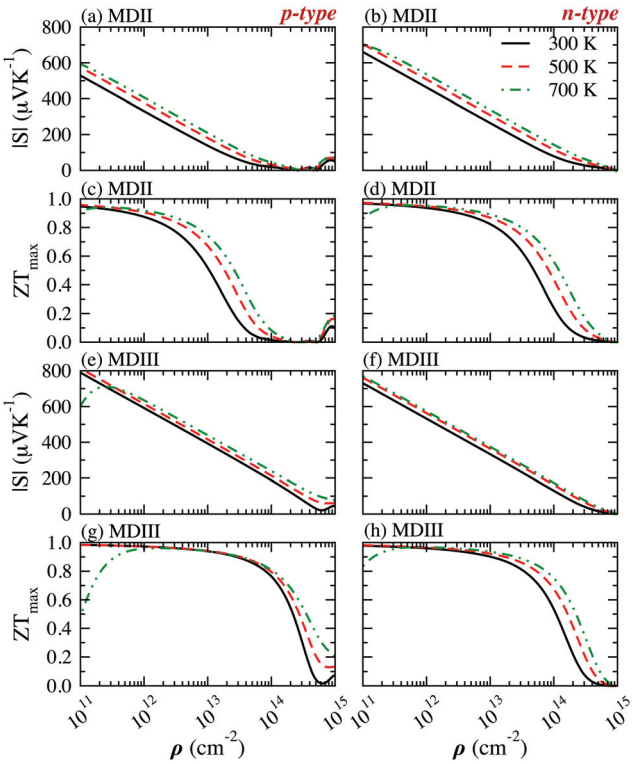

Fig. 5 Seebeck coefficient and maximum TE figure-of-merit as a function of carrier density at T = 300, 500, and 700 K of Zr_2CO_2. Plots for the MD-II and MD-III configurations are represented in a–d and e–h, respectively.

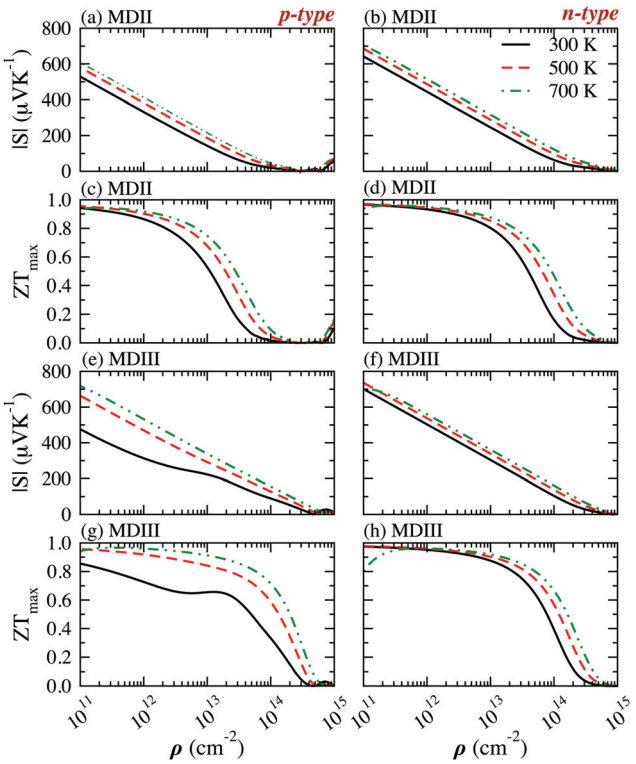

Fig. 6 Seebeck coefficient and maximum TE figure-of-merit as a function of carrier density at T = 300, 500, and 700 K of Hf_2CO_2. Plots for the MD-II and MD-III configurations are represented in a–d and e–h, respectively.

205 μV K^{-1} at T = 300 K, and 608 μV K^{-1} at T = 300 K, respectively.[53–55]

In the case of narrow band gap semiconductors, the minority carriers lead to a decrease in the Seebeck coefficient with an increase in the electrical conductivity at high temperature values and low carrier densities.[56] As the temperature increases, this decrease in the Seebeck coefficient can be prominently seen as shown in Fig. 4(c, d) and (g, h), because of the narrow band gap of Ti_2CO_2. This effect is rather small for Zr, Hf and Sc-based MXenes. The variation of the Seebeck coefficient as a function of carrier concentration is in good agreement with previous calculations.[29]

Based on the definition of zT, a large Seebeck coefficient together with a large ratio between electronic and lattice thermal conductivity give rise to a large zT value. As shown in Fig. 5(c, d, g, h), 6(c, d, g, h) and 7(c, d), for both n-type and p-type carrier concentrations zT_{max} yields values around 0.9–1.0 at moderate charge carrier densities, where the n-type doped monolayers have a slightly larger Seebeck coefficient and zT_{max} values as compared to the p-type doped ones. These zT_{max} results unveil that the studied MXene materials might exhibit TE performance as good as the mostly studied TE materials Bi_2Te_3 and $SrTiO_3$, even though the maximum zT value of each one could not be larger than 1.0. At moderate doping levels, the zT_{max} value is found to be around 0.65 and 0.7 for Bi_2Te_3 and $SrTiO_3$, respectively.[57] Our calculated values

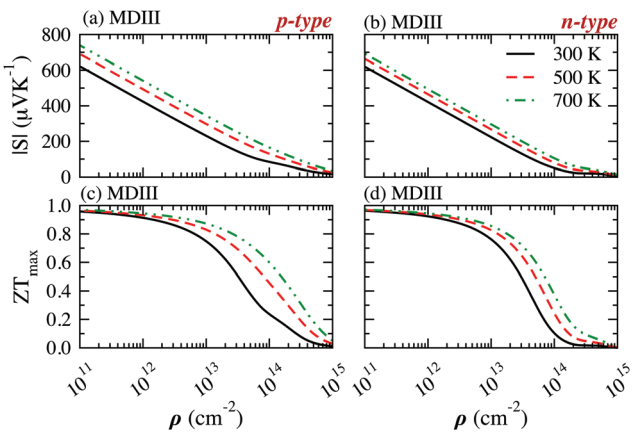

Fig. 7 Seebeck coefficient and maximum TE figure-of-merit as a function of carrier density at T = 300, 500, and 700 K of Sc_2CO_2 for the MD-III configuration.

are also quite promising. Essentially, oxide thermoelectric materials, including n-type $SrTiO_3$,[58] $CaMnO_3$[59] and ZnO[60] and p-type $Ca_3Co_4O_9$[61] and Na_xCoO_2,[62] have various advantages over alloy thermoelectric materials, including their resistance to high temperatures (due to their structural and chemical stability), oxidation resistance, low toxicity, easy processing, and low costs. Nevertheless, due to their very low electrical

conductivity, the zT values of oxides are not high enough as compared with good thermoelectric materials including Bi_2Te_3. In this respect, the semiconducting oxygen terminated MXene monolayers exhibit much better electrical properties due to their electronic structure possessing lower electronic band gap values.

In order to estimate the thermoelectric properties of these materials more realistically, we also investigated lattice thermal transport properties. In Fig. 8(a) and (b), we present the calculated κ_l values of the MD-II and MD-III configurations predicted by iterative solutions of the linearized BTE as a function of temperature, respectively. The first observation is that the MD-III structure of a particular MXene has lower κ_l than its MD-II structure. As shown in Fig. S6–S9 in the ESI,† the ZA branch is softer in MD-III than in MD-II. Due to the reduced crystal symmetry, the ZA mode undergoes enhanced scattering, thereby suppressing the contribution of the ZA mode to the κ_l, see Fig. S11.† Thus, the relaxation time of this mode in MD-III is quite short as compared to that in MD-II, as seen in Fig. S12.† In addition, the contribution of optical phonons to the κ_l is quite large in these two dimensional crystals as compared to graphene[63] and blue phosphorus.[64] Fig. 8(a) and (b) show that the κ_l of MXenes is inversely proportional to temperature (T^{-1}). The temperature dependence of κ_l of the MD-II structure of M_2CO_2 (M = Ti, Zr, Hf) is in line with the values predicted by Gandi *et al.*[29] We found that, in the MD-III structure, the contribution of optical phonons is significantly reduced as compared to the MD-II structure. At room temperature, all these considered materials have much lower κ_l as compared to monolayer graphene (2200 W mK^{-1},[46] 4840–5300 W mK^{-1}[63]) and hBN (360 W mK^{-1}).[65] Furthermore, these MXene materials have as low κ_l as most promising 2D materials for nano-electronic applications such as few-layered MoS_2 (44–103 W mK^{-1}),[66,67] silicene (36.2 W mK^{-1}),[68] black phosphorene (110 W mK^{-1} (armchair) and 36 W mK^{-1} (zigzag)) and blue phosphorene (78 W mK^{-1}).[64]

For the MD-III configuration of Ti_2CO_2 and Zr_2CO_2, the variation of the κ_l with temperature has similar behavior at all temperature values considered here. As can be seen from Fig. 8(b), the κ_l of Sc_2CO_2-MD-III is noticeably higher than the values corresponding to the others for the temperature values below 300 K. The calculated κ_l values at T = 300 K, 500 K and 700 K are given in Table 2. The MD-III configuration of Ti_2CO_2 and Zr_2CO_2 has the lowest κ_l as compared to the others in both MD-II and MD-III configurations. Among all the considered structures, Hf_2CO_2 in the MD-II configuration has the highest κ_l. This higher value partially is a result of the large gap between acoustic and optical phonon branches in its phonon dispersion curve (Fig. S8 in the ESI†) that reduces the three-phonon scattering processes.[69,70] The calculated κ_l of Sc_2CO_2 in MD-III is 47 W mK^{-1} at T = 300 K, consistent with the value of 59 W mK^{-1} reported in a previous study.[71] For the MD-II configuration, the κ_l increases as the atomic number of M (M = Ti, Zr, Hf) increases whereas the MD-III configurations exhibit an abnormal trend, most likely due to the distinct nature of Umklapp scattering processes. A similar result was also predicted for monolayer MoS_2 and WS_2 crystals.[67]

Table 2 The lattice thermal conductivity, κ_l values for the MD-II and MD-III configurations of M_2CO_2 (M = Ti, Zr, Hf, Sc) at T = 300, 500 and 700 K

	T = 300 K		T = 500 K		T = 700 K	
κ (W mK^{-1})	MD-II	MD-III	MD-II	MD-III	MD-II	MD-III
Ti_2CO_2	40.58	18.42	22.29	10.47	15.50	7.36
Zr_2CO_2	50.40	16.85	28.37	9.71	19.88	6.85
Hf_2CO_2	57.39	27.43	31.82	15.69	22.18	11.05
Sc_2CO_2	Metal	47.01	Metal	25.93	Metal	18.06

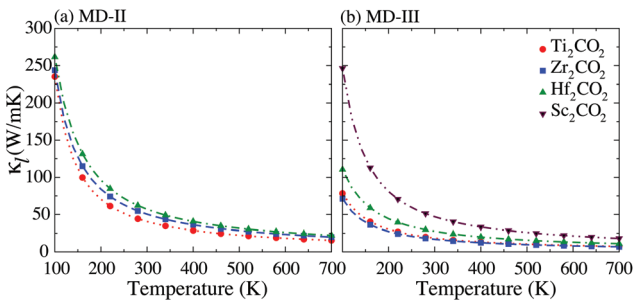

Fig. 8 Lattice thermal conductivity, κ_l values as a function of temperature in the range of 100 K to 700 K for (a) the MD-II and (b) MD-III structures. The ratio of self consistent κ_l values (κ) to RTA solutions (κ_{RTA}) for (c) the MD-II and (d) MD-III structures.

Subsequent to the first principles κ_l calculations, we determined the $zT = S^2\sigma T/(\kappa_e + \kappa_l)$ within constant electronic RTA for both p- and n-type doping. Fig. 9 shows the carrier density dependency of the calculated zT values for each monolayer MXene crystal. Here, the relaxation time of holes and electrons was fixed to 10 fs ($\tau = 10^{-14}$ s^{-1}) as proposed in ref. 25. Because of the fact that the Seebeck coefficient has higher values and also the κ_l has lower values in the MD-III configuration, the zT of the MD-III configurations tends to acquire larger values compared to the MD-II structures. Similar to our assumption of vanishing κ_l, this approximation also puts an upper bound for zT values. zT acquires its maximum attainable value for the charge densities around 10^{13}–10^{14} cm^{-2} for all the considered systems. Our results clearly showed the notable influence of the functionalization on the electronic, thermal, and thermoelectric properties, consistent with the previous findings, which demonstrated the strong influence of functionalization on the electronic properties.[72] The plots of temperature dependent maximum zT values, calculated for τ = 5 fs and 15 fs, are shown in Fig. 10(a) and (b). As expected, the longer relaxation times give rise to larger zT_{max} values. Fig. 10 also demonstrates the importance of surface functionalization discussed above. For instance, while n-type doping yields larger zT_{max} values for all MD-II structures, either n-type or p-type doping may yield larger zT_{max} values depending on the metal type for MD-III structures. In this work, we did not consider the random functionalization of O atoms due to the sig-

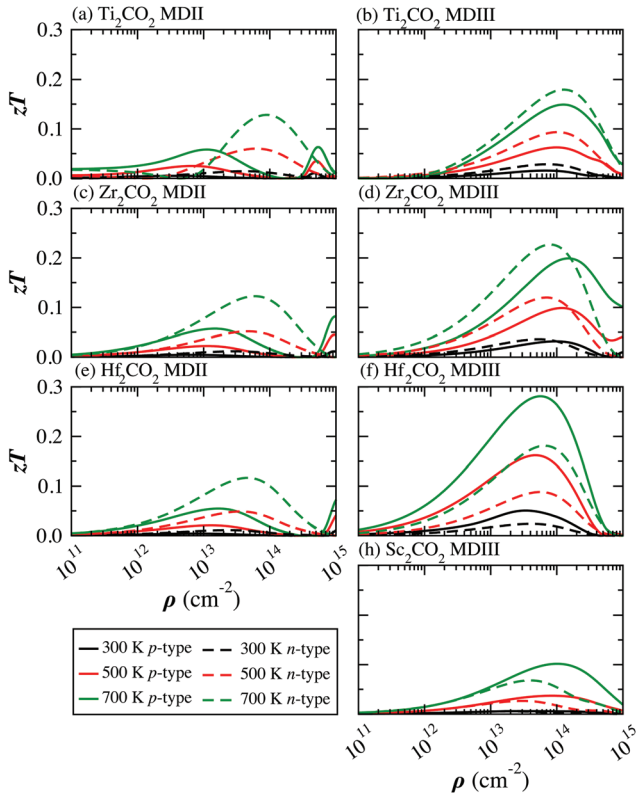

Fig. 9 zT as a function of carrier density using constant relaxation time approximation with τ = 10 fs for p-type and n-type doping.

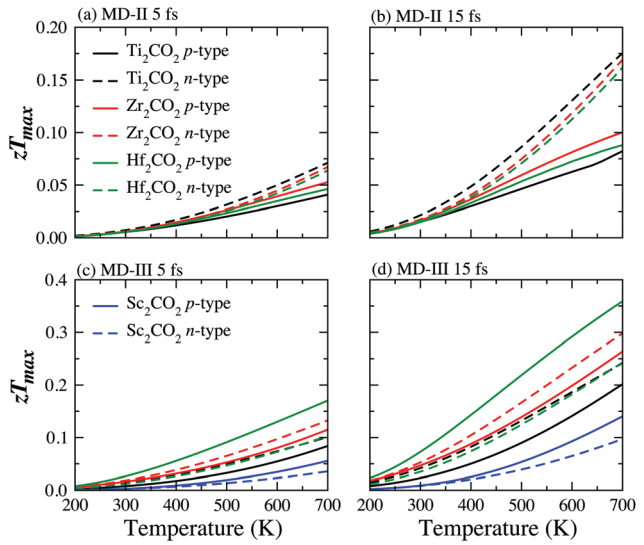

Fig. 10 zT_{max} as a function of temperature using constant relaxation time approximation with τ = 5 fs and τ = 15 fs.

nificant computational cost, in particular in thermal conductivity calculations. However, it is a clear fact that the thermal conductivity can be controlled by the random arrangement, which can affect the thermoelectric properties of the studied materials positively.

Thermoelectric materials require the contradictory properties of high electron mobility, large Seebeck coefficient and low thermal conductivity. High thermoelectric efficiencies can be realized by exploiting different approaches including improving carrier mobility and concentration by doping, enhancing the Seebeck coefficient by band structure engineering, and reducing thermal conductivity by nanostructuring and introducing structural imperfections.[73,74] In this work, we found that lowering the crystal symmetry of MXene monolayers can double the zT values. Similar to the intrinsic defects, the dopant elements create structural imperfections in the lattice of MXene crystals, which are expected to limit the phonon mean free paths significantly and results in a suppressed phonon transport. Since the dominant heat carriers in semiconductors and insulators are phonons, a reduced thermal conductivity and an improved thermoelectric performance can be achieved. In addition, by exploiting doping, we can also enhance electrical conductivity by optimizing carrier concentrations to increase the power factor (*i.e.* $S^2\sigma$). As we have already shown, the acoustic phonon modes with large wavelengths (small wavenumbers) dominate the thermal transport in both MD-II and MD-III structures due to their large group velocities, see ESI.† Therefore, MXene flakes with in-plane dimensions comparable or smaller than mean free paths of main heat carriers lead to enhanced phonon scattering at interfaces and can attain low thermal conductivity values. We can also avoid the excitation of such phonons by adjusting the size of the MXene flakes. Combining this strategy (*i.e.* nanostructuring proposed by Dresselhaus and co-workers[75]) with band structure engineering to optimize the power factor by altering the electronic structure appears as a promising way to enhance the thermoelectric efficiency.

Finally, we discussed the effect of long range electrostatic interactions on the thermal properties. We note that, due to the finite band gap and the presence of mixed ion-covalent bonds, these structures have appreciable Born effective charges. Our calculation showed that such long range electrostatic interactions give rise to a splitting of LO and TO branches. However, this splitting slightly modifies the thermal properties. This is correlated with the fact that the optical branches have very small contribution to κ_l as compared to the acoustic branches. Despite this, it's very likely to be an erroneous assumption to neglect the optical modes due to the fact that the optical modes are crucial to provide channels for acoustic phonon scattering.

4. Conclusion

We investigated the thermal transport properties (Seebeck coefficient, κ_l, TE figure-of-merit) of oxygen-functionalized M_2CO_2 (where M = Ti, Zr, Hf, Sc) MXenes with two different configurations by using phonon Boltzmann transport theory combined with first-principles calculations. Our results

revealed that the MD-III configurations of M_2CO_2 (M = Ti, Zr, Hf, Sc) structures with larger band gaps exhibit larger Seebeck coefficients than M_2CO_2 structures in the MD-II configuration. The MD-II and MD-III configurations of Zr_2CO_2 and Hf_2CO_2 exhibit nearly the same TE properties whereas the same configurations of Ti_2CO_2 have very distinct TE properties. The effect of the structural model on the TE properties is the largest in Ti_2CO_2. Ti_2CO_2 in the MD-II structure possesses weaker TE efficiency than other structures because of having the lowest Seebeck coefficient values. At room temperature, monolayer Sc_2CO_2 with the MD-III configuration has the maximum Seebeck coefficient. The TE performance of the MD-II structures is generally weak at room temperature, because of having relatively larger κ_l and smaller Seebeck coefficient. The calculated κ_l values are much lower than that of graphene whereas they are comparable to those of MoS_2, silicene and phosphorene. We also found that the largest contribution to κ_l is given by acoustic phonons. Due to the enhanced scattering of the ZA mode as a result of reduced crystal symmetry, the MD-III structures have lower κ_l as compared to the MD-II ones. The contribution of each phonon mode to κ_l, relaxation time and MFP provides great guidance to experimental efforts and also sheds light on nanodesigning of MXene based TE materials. The structural variety provides us an additional degree of freedom for modulating physical and chemical properties of MXenes, which can be exploited to design efficient thermoelectric devices.

Conflicts of interest

There are no conflicts to declare.

Acknowledgements

We acknowledge the support from the Scientific and Technological Research Council of Turkey (TUBITAK-116F080). A part of this work was supported by the BAGEP Award of the Science Academy. Computational resources were provided by TUBITAK ULAKBIM, High Performance and Grid Computing Center (TRGrid e-Infrastructure) and Istanbul Technical University, National Center for High Performance Computing (UHeM). This work was performed, in part, at the Center for Nanoscale Materials, a U.S. Department of Energy Office of Science User Facility, and supported by the U.S. Department of Energy, Office of Science, under contract no. DE-AC02-06CH11357.

References

1 K. S. Novoselov, A. K. Geim, S. V. Morozov, D. Jiang, Y. Zhang, S. V. Dubonos, I. V. Grigorieva and A. A. Firsov, *Science*, 2004, **306**(5696), 666–669.
2 M. Naguib, O. Mashtalir, J. Carle, V. Presser, J. Lu, L. Hultman, Y. Gogotsi and M. W. Barsoum, *ACS Nano*, 2012, **6**(2), 1322–1331.
3 M. Naguib, M. Kurtoglu, V. Presser, J. Lu, J. Niu, M. Heon, L. Hultman, Y. Gogotsi and M. W. Barsoum, *Adv. Mater.*, 2011, **23**(37), 4248–4253.
4 M. Naguib, J. Halim, J. Lu, K. M. Cook, L. Hultman, Y. Gogotsi and M. W. Barsoum, *J. Am. Chem. Soc.*, 2013, **135**(43), 15966–15969.
5 M. Ghidiu, M. Naguib, C. Shi, O. Mashtalir, L. M. Pan, B. Zhang, J. Yang, Y. Gogotsi, S. J. L. Billingeb and M. W. Barsoum, *Chem. Commun.*, 2014, **50**(67), 9517–9520.
6 R. Meshkian, L.-A. Naslund, J. Halim, J. Lu, M. W. Barsoum and J. Rosen, *Scr. Mater.*, 2015, **108**, 147–150.
7 B. Anasori, Y. Xie, M. Beidaghi, J. Lu, B. C. Hosler, L. Hultman, P. R. C. Kent, Y. Gogotsi and M. W. Barsoum, *ACS Nano*, 2015, **9**(10), 9507–9516.
8 P. Urbankowski, B. Anasori, T. Makaryan, D. Er, S. Kota, P. L. Walsh, M. Zhao, V. B. Shenoy, M. W. Barsouma and Y. Gogotsi, *Nanoscale*, 2016, **8**(22), 11385–11391.
9 M. Naguib, J. Come, B. Dyatkin, V. Presser, P.-L. Taberna, P. Simon, M. Barsoum and Y. Gogotsi, *Electrochem. Commun.*, 2012, **16**(1), 61–64.
10 H. Liu, D. Su, R. Zhou, B. Sun, G. Wang and S. Z. Qiao, *Adv. Energy Mater.*, 2012, **2**(8), 970–975.
11 Q. Tang, Z. Zhou and P. Shen, *J. Am. Chem. Soc.*, 2012, **134**(40), 16909–16916.
12 D. Er, J. Li, M. Naguib, Y. Gogotsi and V. B. Shenoy, *ACS Appl. Mater. Interfaces*, 2014, **6**(14), 11173–11179.
13 M. R. Lukatskaya, O. Mashtalir, C. E. Ren, Y. DallAgnese, P. Rozier, P. L. Taberna, M. Naguib, P. Simon, M. W. Barsoum and Y. Gogotsi, *Science*, 2013, **341**(6153), 1502–1505.
14 M. Ghidiu, M. R. Lukatskaya, M.-Q. Zhao, Y. Gogotsi and M. W. Barsoum, *Nature*, 2014, **516**(7529), 78–81.
15 H. Tang, J. Wang, H. Yin, H. Zhao, D. Wang and Z. Tang, *Adv. Mater.*, 2015, **27**(6), 1117–1123.
16 M. Naguib, V. Mochalin, M. Barsoum and Y. Gogotsi, *Adv. Mater.*, 2014, **26**(7), 992–1005.
17 Q. Hu, D. Sun, Q. Wu, H. Wang, L. Wang, B. Liu, A. Zhou and J. He, *J. Phys. Chem. A*, 2013, **117**(51) 14253–14260.
18 Q. Hu, H. Wang, Q. Wu, X. Ye, A. Zhou, D. Sun, L. Wang, B. Liu and J. He, *Int. J. Hydrogen Energy*, 2014, **39**(20), 10606–10612.
19 L.-Y. Gan, Y.-J. Zhao, D. Huang and U. Schwingenschlgl, *Phys. Rev. B: Condens. Matter Mater. Phys.*, 2013, **87**(24), 245307.
20 Z. Ma, Z. Hu, X. Zhao, Q. Tang, D. Wu, Z. Zhou and L. Zhang, *J. Phys. Chem. C*, 2014, **118**(10), 5593–5599.
21 H. Kim, B. Anasori, Y. Gogotsi and H. N. Alshareef, *Chem. Mater.*, 2017, **29**, 6472–6479.
22 M. Khazaei, M. Arai, T. Sasaki, C. Y. Chung, N. S. Venkataramanan, M. Estili, Y. Sakka and Y. Kawazoe, *Adv. Funct. Mater.*, 2013, **23**(17), 2185–2192.

23 X.-H. Zha, K. Luo, Q. Li, Q. Huang, J. He, X. Wen and S. Du, *Europhys. Lett.*, 2015, **111**(2), 26007.
24 Q. Peng, J. Guo, Q. Zhang, J. Xiang, B. Liu, A. Zhou, R. Liu and Y. Tian, *J. Am. Chem. Soc.*, 2014, **136**(11), 4113–4116.
25 M. Khazaei, M. Arai, T. Sasaki, M. Estili and Y. Sakka, *Phys. Chem. Chem. Phys.*, 2014, **16**(17), 7841–7849.
26 Y. Xie, M. Naguib, V. N. Mochalin, M. W. Barsoum, Y. Gogotsi, X. Yu, K.-W. Nam, X.-Q. Yang, A. I. Kolesnikov and P. R. C. Kent, *J. Am. Chem. Soc.*, 2014, **136**(17), 6385–6394.
27 X.-H. Zha, J. Zhou, Y. Zhou, Q. Huang, J. He, J. S. Francisco, K. Luo and S. Du, *Nanoscale*, 2016, **8**(11), 6110–6117.
28 X.-H. Zha, Q. Huang, J. He, H. He, J. Zhai, J. S. Francisco and S. Dua, *Sci. Rep.*, 2016, **6**, 27971.
29 A. N. Gandi, H. N. Alshareef and U. Schwingenschlgl, *Chem. Mater.*, 2016, **28**(6), 1647–1652.
30 U. Yorulmaz, A. Özden, N. K. Perkgöz, F. Ay and C. Sevik, *Nanotechnology*, 2016, **27**(33), 335702.
31 M. Omini and A. Sparavigna, *Phys. B*, 1995, **212**, 101–112.
32 D. Nika, E. Pokatilov, A. Askerov and A. Balandin, *Phys. Rev. B: Condens. Matter Mater. Phys.*, 2009, **79**, 155413.
33 D. Nika, S. Ghosh, E. Pokatilov and A. Balandin, *Appl. Phys. Lett.*, 2009, **94**, 203103.
34 G. Kresse and J. Hafner, *Phys. Rev. B: Condens. Matter Mater. Phys.*, 1993, **47**(1), 558.
35 G. Kresse and J. Hafner, *Phys. Rev. B: Condens. Matter Mater. Phys.*, 1994, **49**(20), 14251.
36 J. P. Perdew, K. Burke and M. Ernzerhof, *Phys. Rev. Lett.*, 1996, **77**, 3865.
37 H. J. Monkhorst and J. D. Pack, *Phys. Rev. B: Solid State*, 1976, **13**, 5188–5192.
38 J. Ziman, *Electrons and Phonons: The Theory of Transport Phenomena in Solids*, Oxford University Press, 1960.
39 W. Li, J. Carrete, N. A. Katcho and N. Mingo, *Comput. Phys. Commun.*, 2014, **185**(6), 1747–1758.
40 A. Togo and I. Tanaka, *Scr. Mater.*, 2015, **108**, 1–5.
41 L.-Y. Gan, D. Huang and U. Schwingenschlogl, *J. Mater. Chem. A*, 2013, **1**, 13672–13678.
42 G. K. Madsen and D. J. Singh, *Comput. Phys. Commun.*, 2006, **175**(1), 67–71.
43 Y. Xie and P. Kent, *Phys. Rev. B: Condens. Matter Mater. Phys.*, 2013, **87**, 235441.
44 G. Wang and T. Cagin, *Phys. Rev. B: Condens. Matter Mater. Phys.*, 2007, **76**, 075201.
45 L.-D. Zhao, G. Tan, S. Hao, J. He, Y. Pei, H. Chi, H. Wang, S. Gong, H. Xu, V. P. Dravid, C. Uher, G. J. Snyder, C. Wolverton and M. G. Kanatzidis, *Science*, 2016, **351**, 141–144.
46 B. D. Kong, S. Paul, M. B. Nardelli and K. W. Kim, *Phys. Rev. B: Condens. Matter Mater. Phys.*, 2009, **80**, 033406.
47 G. Qin, Q.-B. Yan, Z. Qin, S.-Y. Yue, M. Hu and G. Su, *Phys. Chem. Chem. Phys.*, 2015, **17**, 4854–4858.
48 B. Peng, H. Zhang, H. Shao, Y. Xu, X. Zhang and H. Zhu, *Sci. Rep.*, 2016, **6**, 20225.
49 N. Bonini, J. Garg and N. Marzari, *Nano Lett.*, 2012, **12**, 2673–2678.
50 G. Fugallo, A. Cepellotti, L. Paulatto, M. Lazzeri, N. Marzari and F. Mauri, *Nano Lett.*, 2014, **14**, 6109–6114.
51 J. Carrete, W. Li, L. Lindsay, D. A. Broido, L. J. Gallego and N. Mingo, *Mater. Res. Lett.*, 2016, **4**, 204–211.
52 S. Ghosh, W. Bao, D. L. Nika, S. Subrina, E. P. Pokatilov, C. N. Lau and A. A. Balandin, *Nat. Mater.*, 2010, **9**, 555–558.
53 H. Ohta, S. Kim, Y. Mune, T. Mizoguchi, K. Nomura, S. Ohta, T. Nomura, Y. Nakanishi, Y. Ikuhara, M. Hirano, *et al.*, *Nat. Mater.*, 2007, **6**, 129–134.
54 G. Zhang, B. Kirk, L. A. Jauregui, H. Yang, X. Xu, Y. P. Chen and Y. Wu, *Nano Lett.*, 2011, **12**, 56–60.
55 G. Zhang, H. Fang, H. Yang, L. A. Jauregui, Y. P. Chen and Y. Wu, *Nano Lett.*, 2012, **12**, 3627–3633.
56 A. F. May, M. A. McGuire, D. J. Singh, J. Ma, O. Delaire, A. Huq, W. Cai and H. Wang, *Phys. Rev. B: Condens. Matter Mater. Phys.*, 2012, **85**, 035202.
57 C. Sevik and T. Çağın, *Phys. Rev. B: Condens. Matter Mater. Phys.*, 2010, **82**, 045202.
58 S. Ohta, T. Nomura, H. Ohta and K. Koumoto, *J. Appl. Phys.*, 2005, **97**, 034106.
59 D. Flahaut, T. Mihara, R. Funahashi, N. Nabeshima, K. Lee, H. Ohta and K. Koumoto, *J. Appl. Phys.*, 2006, **100**, 084911.
60 Y. Yin, B. Tudu and A. Tiwari, *Vacuum*, 2017, **146**, 356–374.
61 R. Funahashi, I. Matsubara, H. Ikuta, T. Takeuchi, U. Mizutani and S. Sodeoka, *Jpn. J. Appl. Phys.*, 2000, **39**, L1127.
62 I. Terasaki, Y. Sasago and K. Uchinokura, *Phys. Rev. B: Condens. Matter Mater. Phys.*, 1997, **56**, R12685.
63 A. A. Balandin, S. Ghosh, W. Bao, I. Calizo, D. Teweldebrhan, F. Miao and C. N. Lau, *Nano Lett.*, 2008, **8**, 902–907.
64 A. Jain and A. J. McGaughey, *Sci. Rep.*, 2015, **5**, 8501.
65 I. Jo, M. T. Pettes, J. Kim, K. Watanabe, T. Taniguchi, Z. Yao and L. Shi, *Nano Lett.*, 2013, **13**, 550–554.
66 I. Jo, M. T. Pettes, E. Ou, W. Wu and L. Shi, *Appl. Phys. Lett.*, 2014, **104**, 201902.
67 B. Peng, H. Zhang, H. Shao, Y. Xu, X. Zhang and H. Zhu, *RSC Adv.*, 2016, **6**, 5767–5773.
68 H. Xie, T. Ouyang, E. Germaneau, G. Qin, M. Hu and H. Bao, *Phys. Rev. B: Condens. Matter Mater. Phys.*, 2016, **93**, 075404.
69 A. Jain and A. J. McGaughey, *J. Appl. Phys.*, 2014, **116**, 073503.
70 T. Feng and X. Ruan, *J. Nanomater.*, 2014, **2014**, 1–25.
71 S. Kumar and U. Schwingenschlögl, *Phys. Rev. B: Condens. Matter Mater. Phys.*, 2016, **94**, 035405.
72 B. Anasori, M. R. Lukatskaya and Y. Gogotsi, *Nat. Rev. Mater.*, 2017, **2**, 16098.
73 C.-C. Lin, R. Lydia, J. H. Yun, H. S. Lee and J. S. Rhyee, *Chem. Mater.*, 2017, **29**, 5344–5352.
74 T. Zhu, Y. Liu, C. Fu, J. P. Heremans, J. G. Snyder and X. Zhao, *Adv. Mater.*, 2017, **29**, 1605884–1605909.
75 M. S. Dresselhaus, G. Chen, M. Y. Tang, R. G. Yang, H. Lee, D. Z. Wang, Z. F. Ren, J.-P. Fleurial and P. Gogna, *Adv. Mater.*, 2007, **19**, 1043–1053.

Influence of surface functionalization on thermal transport and thermoelectric properties of MXene monolayers.

S. Sarikurt[1], D. Cakir[2], M. Keceli[3], and C. Sevik[4]
[1]Department of Physics, Faculty of Science, Dokuz Eylul University, Izmir, 35390, TURKEY
[2]Department of Physics and Astrophysics, University of North Dakota, Grand Forks, North Dakota 58202, USA
[3]Chemical Sciences and Engineering Division, Argonne National Laboratory, Argonne, Illinois 60439, USA
[4]Department of Mechanical Engineering, Faculty of Engineering, Anadolu University, Eskisehir, 26555, TURKEY

1. Band Structures

1.1. Ti_2CO_2

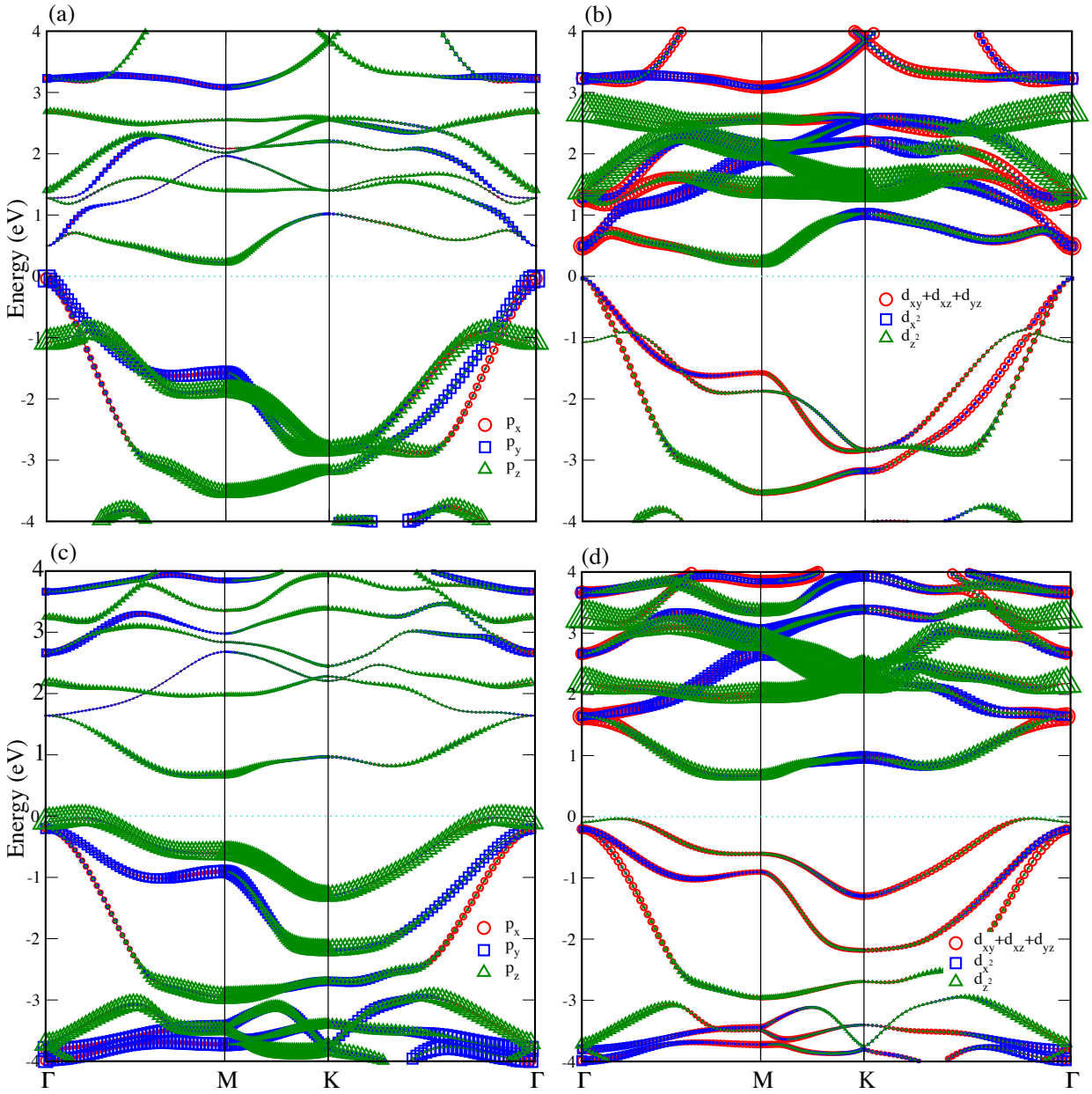

Figure S1: Atomic orbital weights in the energy bands of Ti_2CO_2. *p* and *d* orbital weights for Model II are depicted in (a) and (b). *p* and *d* orbital weights for Model III are depicted in (c) and (d). The size of each

symbol is proportional to the weight of the atomic orbital. Spin orbit coupling (SOC) was neglected in these calculations.

1.2. Zr_2CO_2

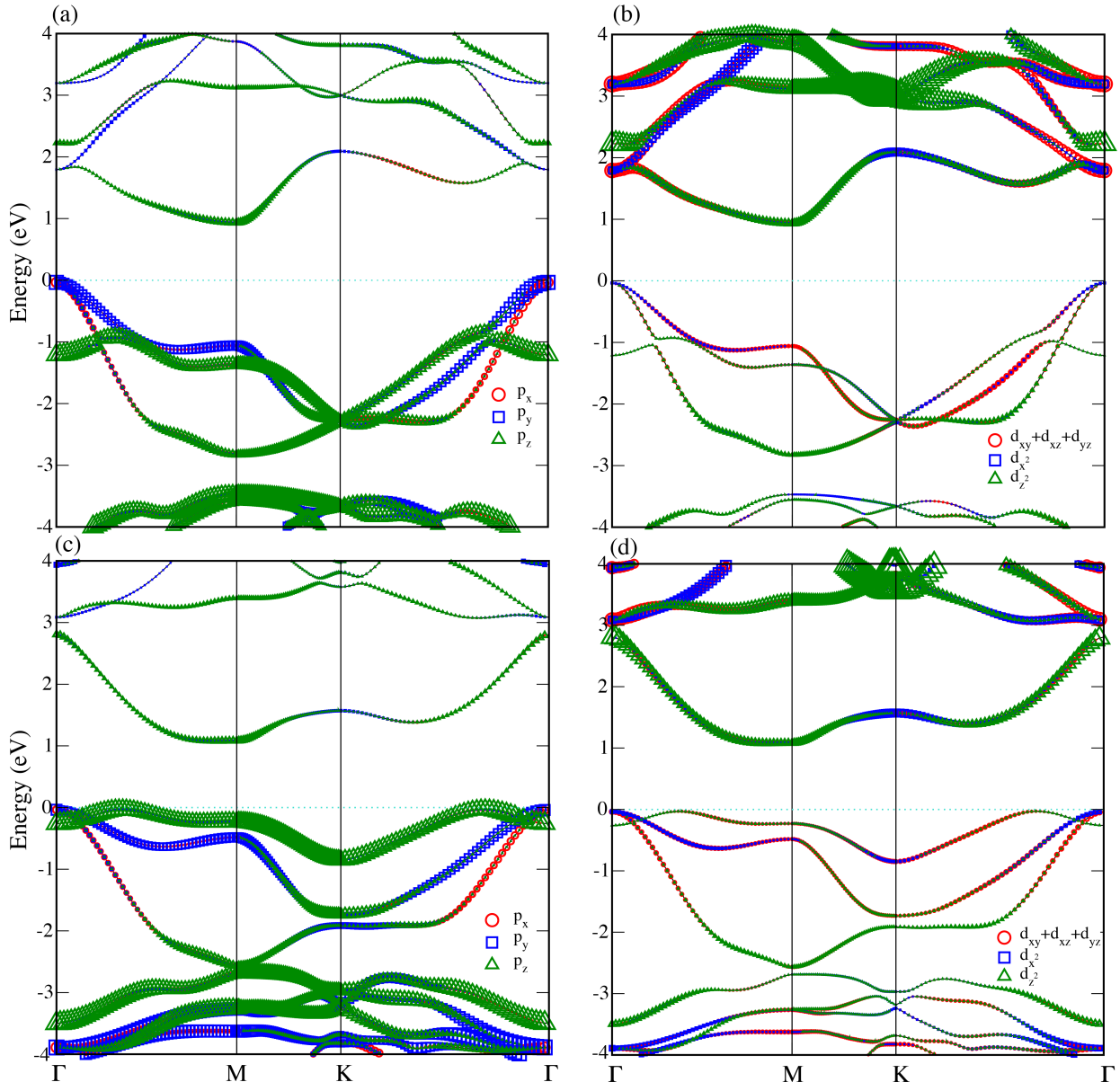

Figure S2: Atomic orbital weights in the energy bands of Zr_2CO_2. *p* and *d* orbital weights for Model II are depicted in (a) and (b). *p* and *d* orbital weights for Model III are depicted in (c) and (d). The size of each symbol is proportional to the weight of the atomic orbital. SOC was neglected in these calculations.

1.3. Hf_2CO_2

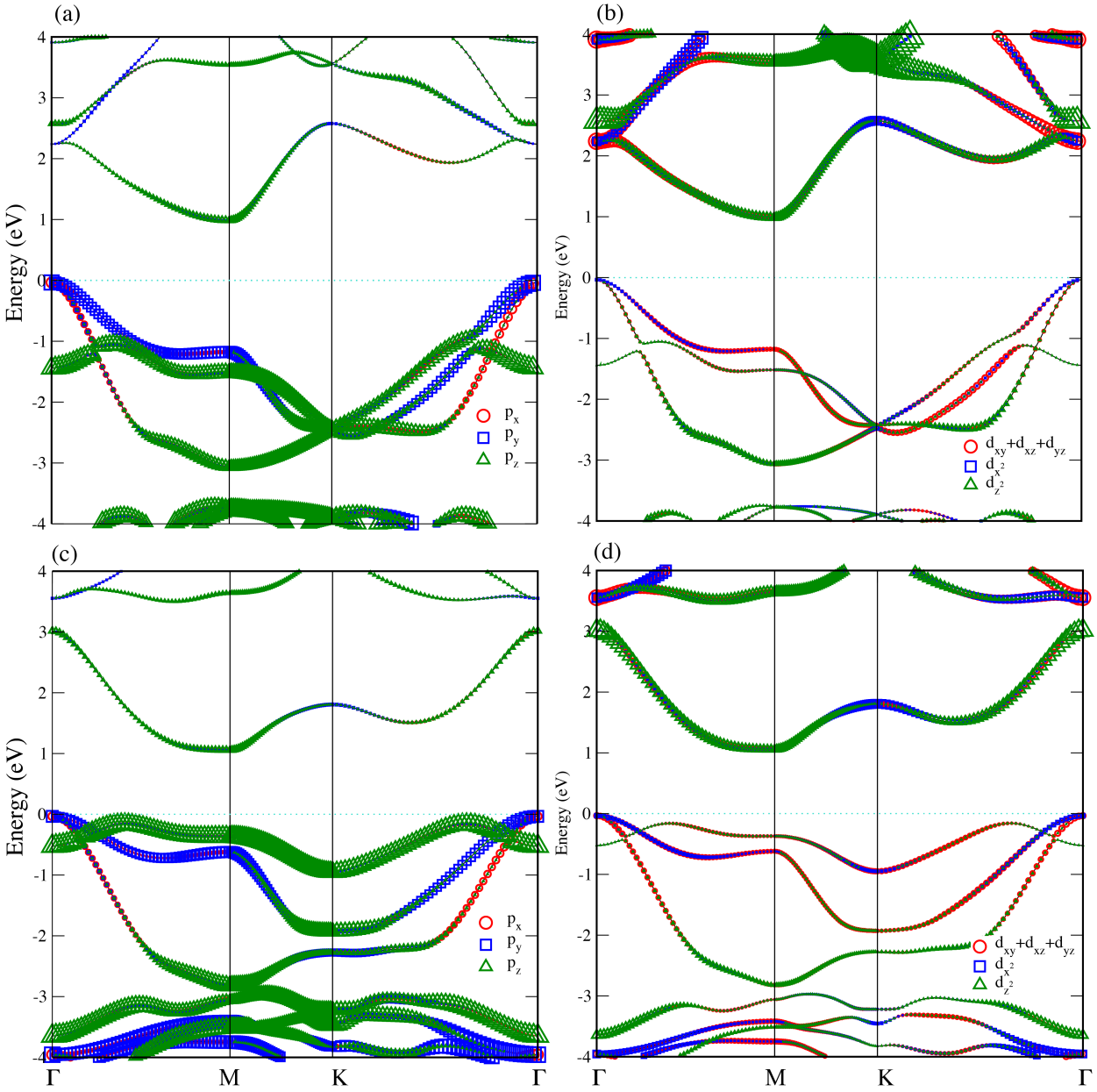

Figure S3: Atomic orbital weights in the energy bands of Hf_2CO_2. *p* and *d* orbital weights for Model II are depicted in (a) and (b). *p* and *d* orbital weights for Model III are depicted in (c) and (d). The size of each symbol is proportional to the weight of the atomic orbital. SOC was neglected in these calculations.

1.4. Sc_2CO_2

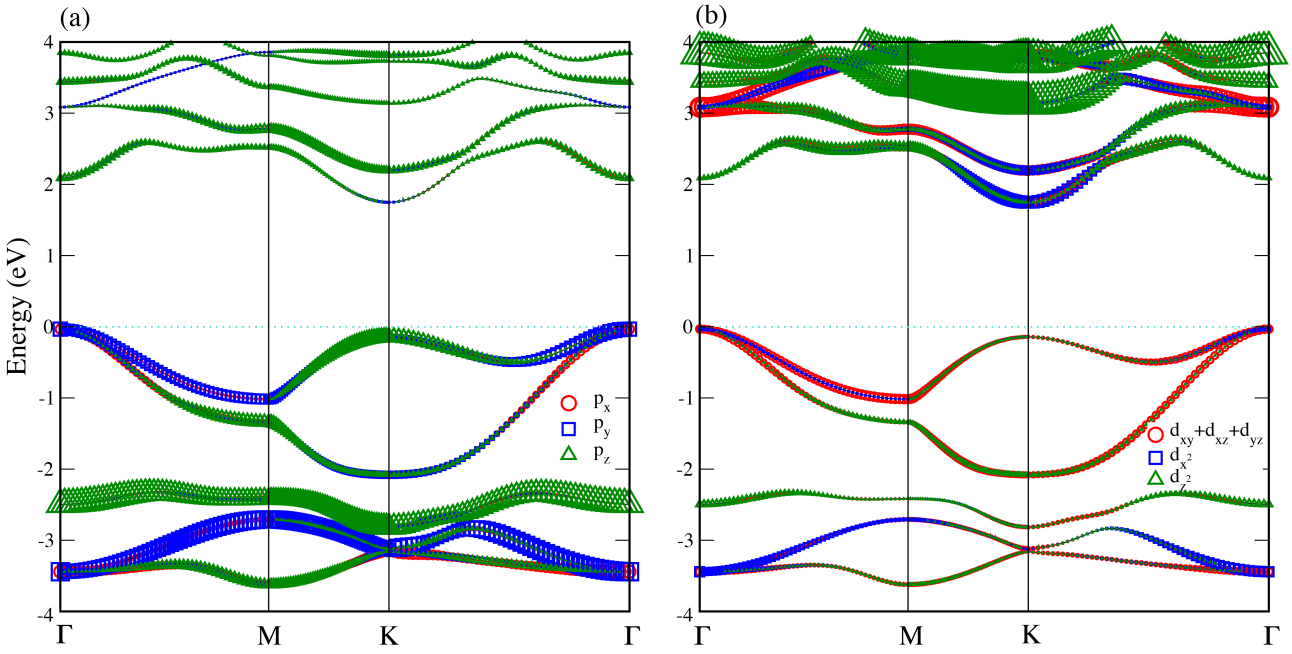

Figure S4: Atomic orbital weights in the energy bands of Sc_2CO_2. *p* and *d* orbital weights for Model III are depicted in (a) and (b). The size of each symbol is proportional to the weight of the atomic orbital. SOC was neglected in these calculations.

2. Density of States

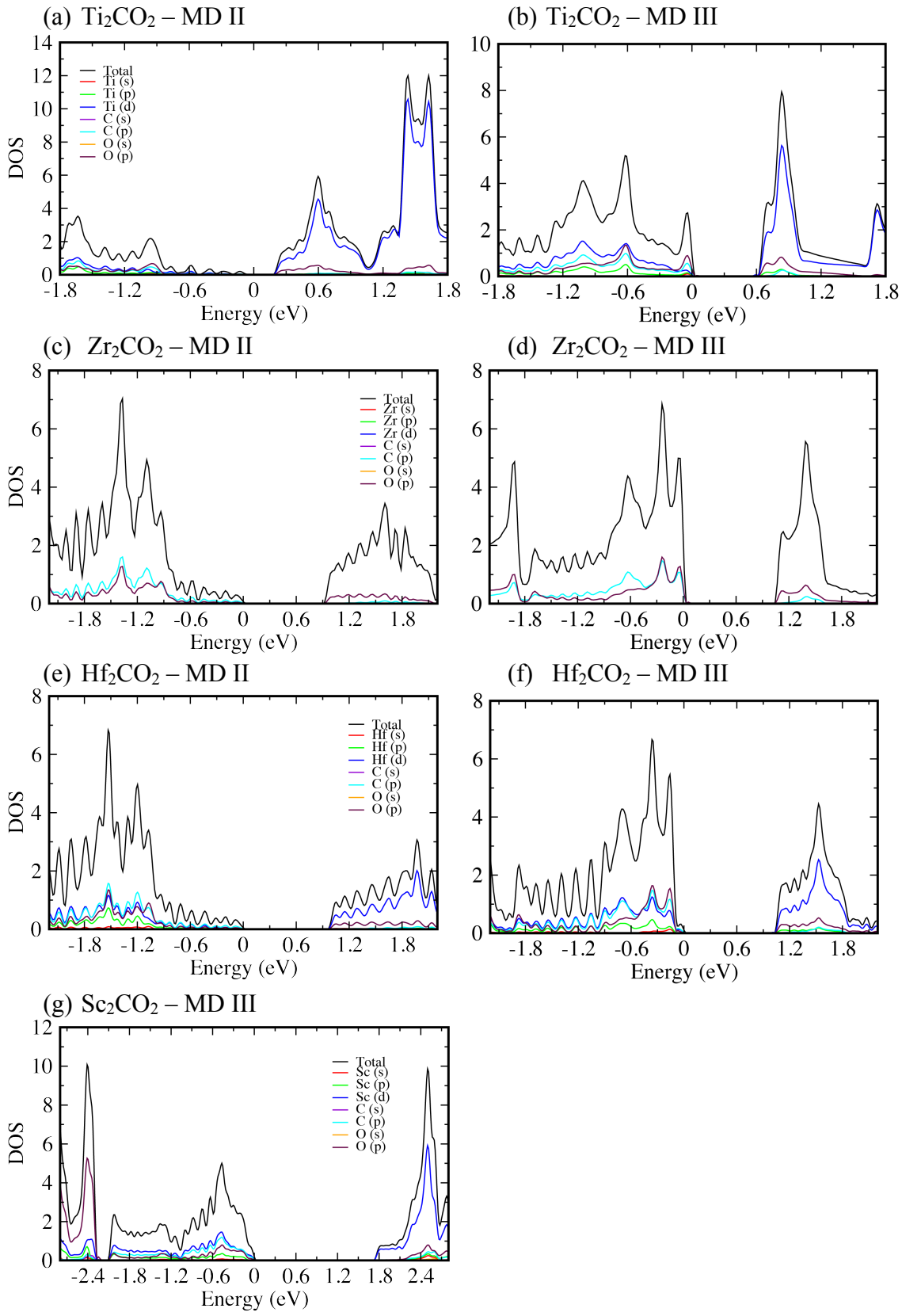

Figure S5: Total density of states and partial density of states of each atom composing (a) Ti_2CO_2 MD-II (b) Ti_2CO_2 MD-III c) Zr_2CO_2 MD-II (d) Zr_2CO_2 MD-III e) Hf_2CO_2 MD-II (f) Hf_2CO_2 MD-III g) Sc_2CO_2 MD-III.

3. Phonon Dispersions

3.1. Ti_2CO_2

(a) MD-II (b) MD-III

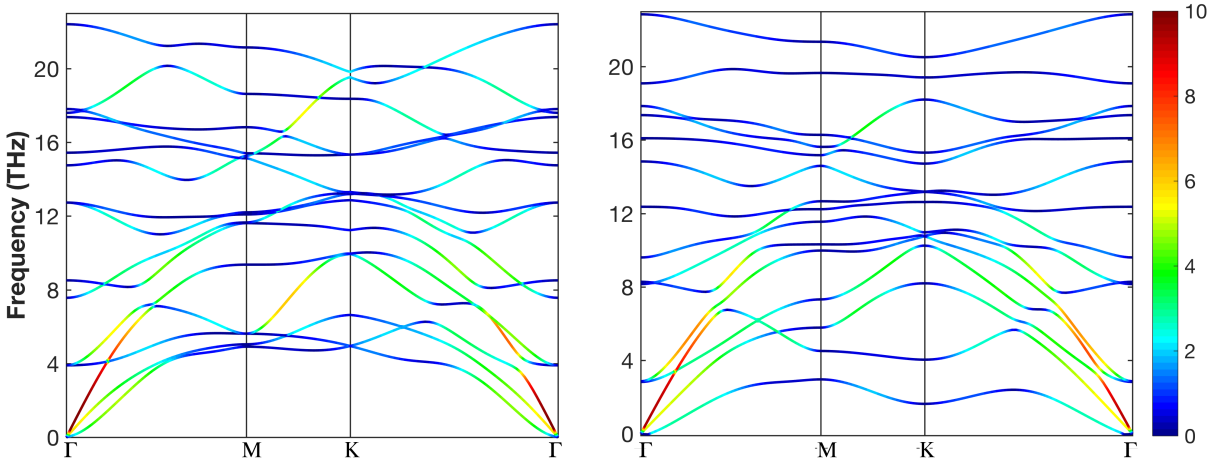

Figure S6: Phonon dispersion curve of Ti_2CO_2 monolayer in (a) MD-II and (b) MD-III configuration. Color bar represent the calculated group velocity in km/h.

3.2. Zr_2CO_2

(a) MD-II (b) MD-III

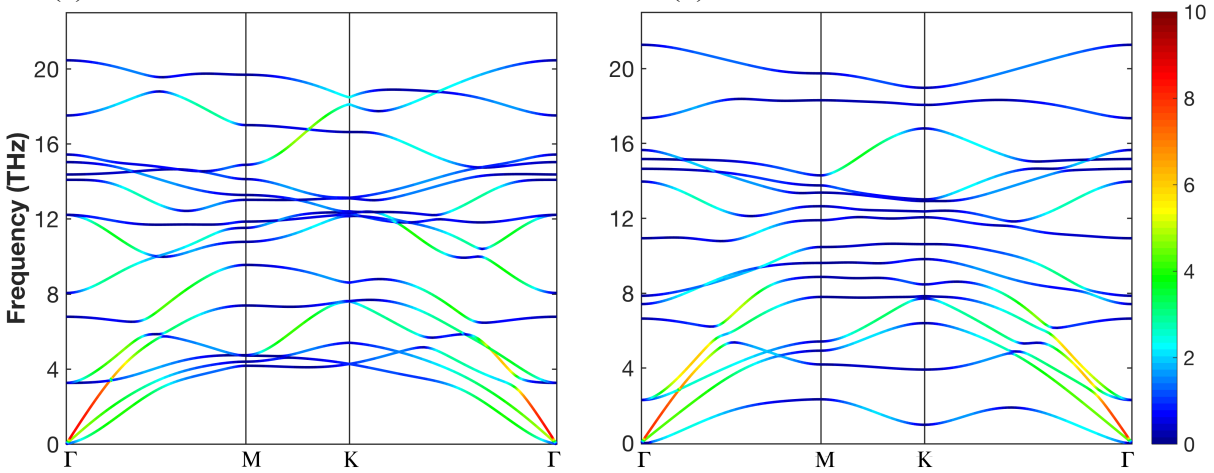

Figure S7: Phonon dispersion curves of Zr_2CO_2 monolayer in (a) MD-II and (b) MD-III configuration. Colour bar represent the calculated group velocity in km/h.

3.3. Hf_2CO_2

(a) MD-II (b) MD-III

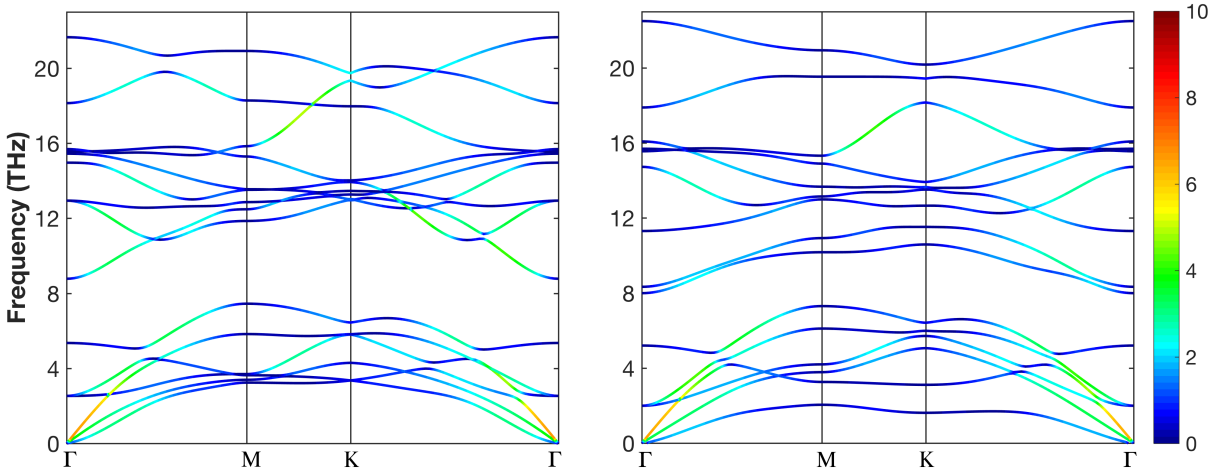

Figure S8: Phonon dispersion curves of Hf_2CO_2 monolayer in (a) MD-II and (b) MD-III configuration. Colour bar represent the calculated group velocity in km/h.

3.4. Sc_2CO_2

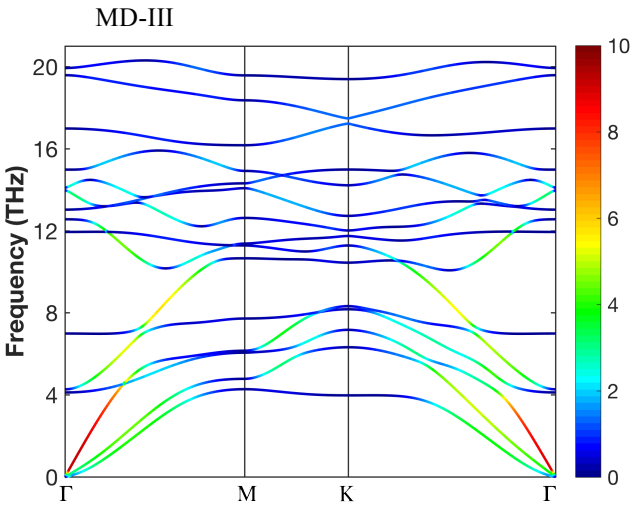

Figure S9: Phonon dispersion curve of Sc_2CO_2 monolayer in MD-III configuration. Colour bar represent the calculated group velocity in km/h.

4. Thermal Properties

4.1. Relaxation Time Approximation

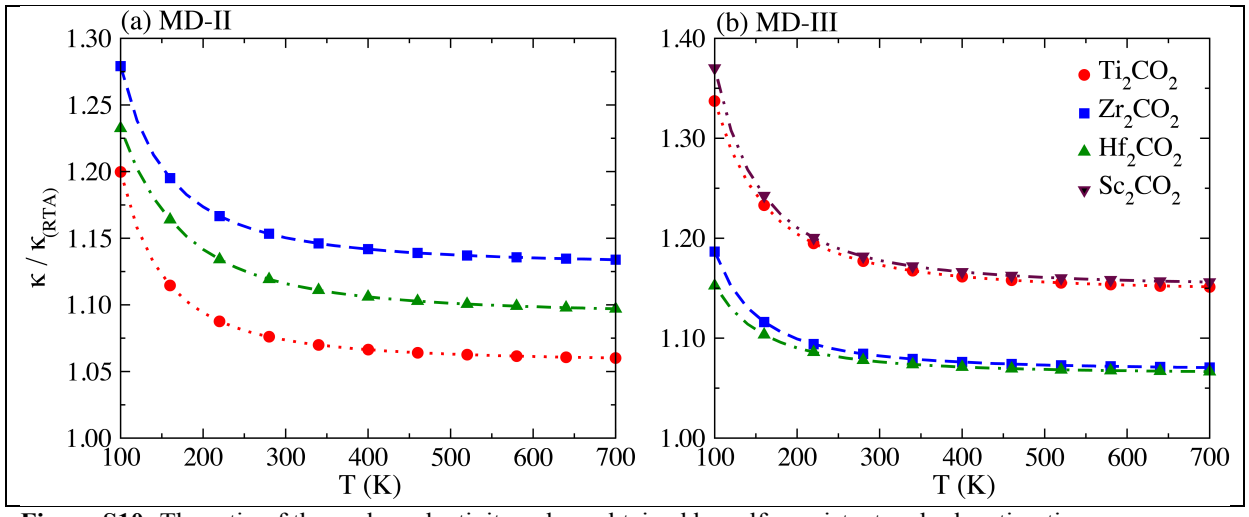

Figure S10: The ratio of thermal conductivity values obtained by self-consistent and relaxation time approximation solutions for (a) MD-II and (b) MD-III structures.

In general, the difference between Relaxation Time Approximation (RTA) and Iterative Solution (IS) is on the order of 10% for 3D materials, but it becomes considerably large for 2D materials. Figure S10 (a) and (b) show the ratio of thermal conductivities calculated using RTA and IS. As shown in these figures, RTA and IS predict quite different TC values, especially, for low temperature values. This is because RTA always severely underestimates TC when the normal scattering (being dominant at low temperature) is strong, which can cause the repopulation of phonon states. At 300 K, the under-prediction is by a factor of around 1.08-1.18 for both MD-II and MD-III configurations. Lindsay *et al.*~\cite reported this under-prediction by a factor of 5 for single-layer graphene at 300 K. Nevertheless, it works reasonably well when Umklapp scattering (being dominant at high temperature) is strong. Therefore, we have a much better agreement at high temperatures, meaning that three phonons

scattering mechanisms are dominated by the Umklapp process. The calculated TC values based on IS are greater than RTA values and the ratio of TC has no significant dependency on temperature above room temperature (300 K). This is because of fact that the presence of low lying optical modes enhances Umklapp scattering involving an optical and an acoustic mode.

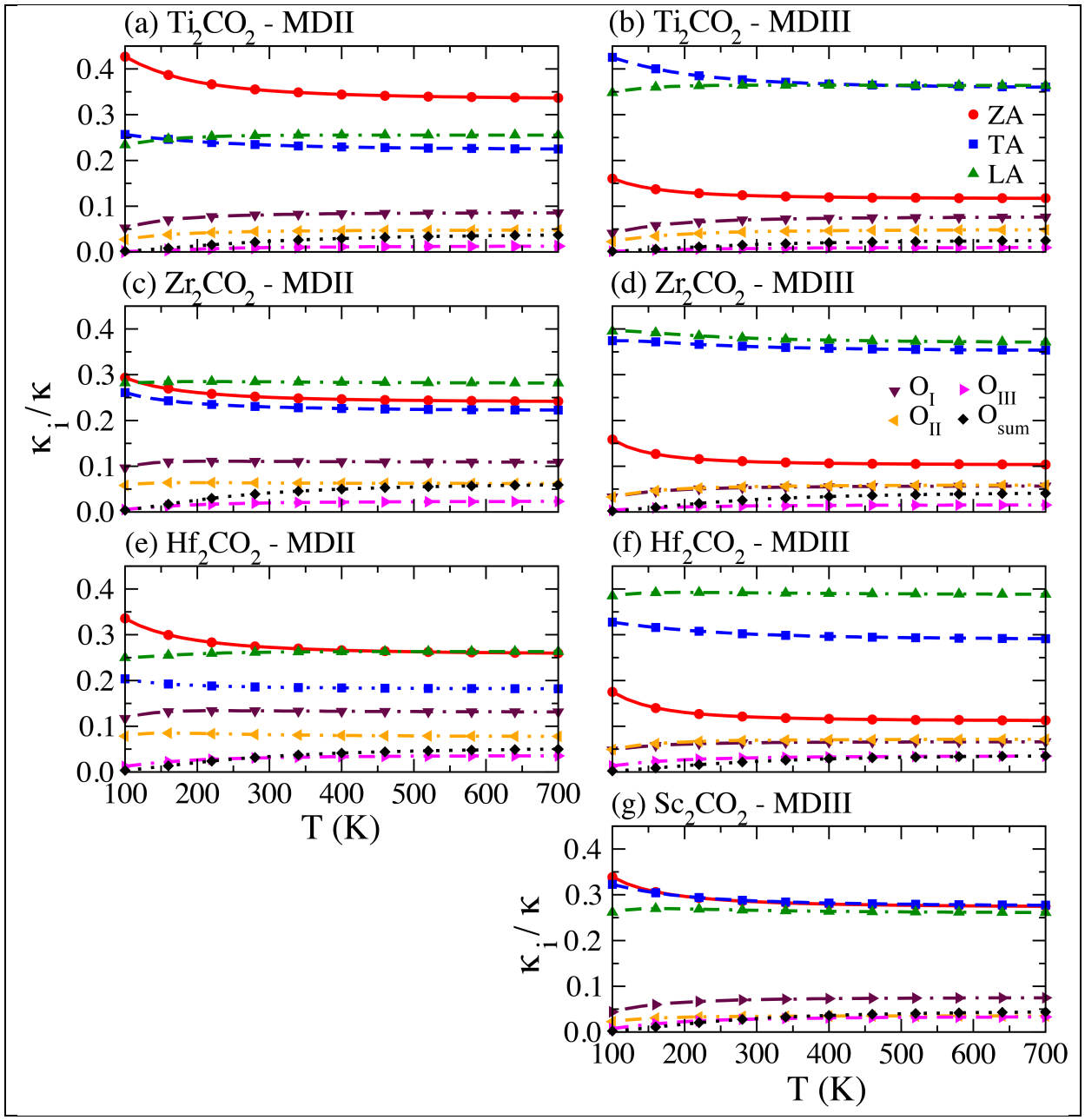

Figure S11: Contribution of phonon modes of functionalized MXene structures to the total lattice thermal conductivity.

The Figure S11 shows the ratio of thermal conductivity (TC) of three acoustic modes (denoted as ZA, TA, LA) and three lowest optical modes (denoted as O_I, O_{II}, O_{III}) to the total lattice TC. The sum of the remaining optical modes O_{sum} is also shown in the same figure. In the case of MD-II configurations, the contribution of ZA branch to the TC is generally larger than that of TA and LA branches. The LA mode gives prominently higher contributions to the total lattice TC in MD-III structures. Interestingly, the contribution of the ZA mode is significantly suppressed in MD-III configuration of M_2CO_2 (M=Ti, Zr, Hf) due to downward

shift of this branch (Figs. S6-S8). The lattice TC is mostly contributed by acoustic modes (more than 70% of the total lattice TC at room temperature) as compared to the optical modes. The optical modes provide more contribution to the total lattice TC in MD-II than in MD-III. Furthermore, the contribution of the acoustic and optical branches become less sensitive (nearly independent) to temperature above 300 K, meaning that all phonon modes are already excited when temperature exceeds 300 K.

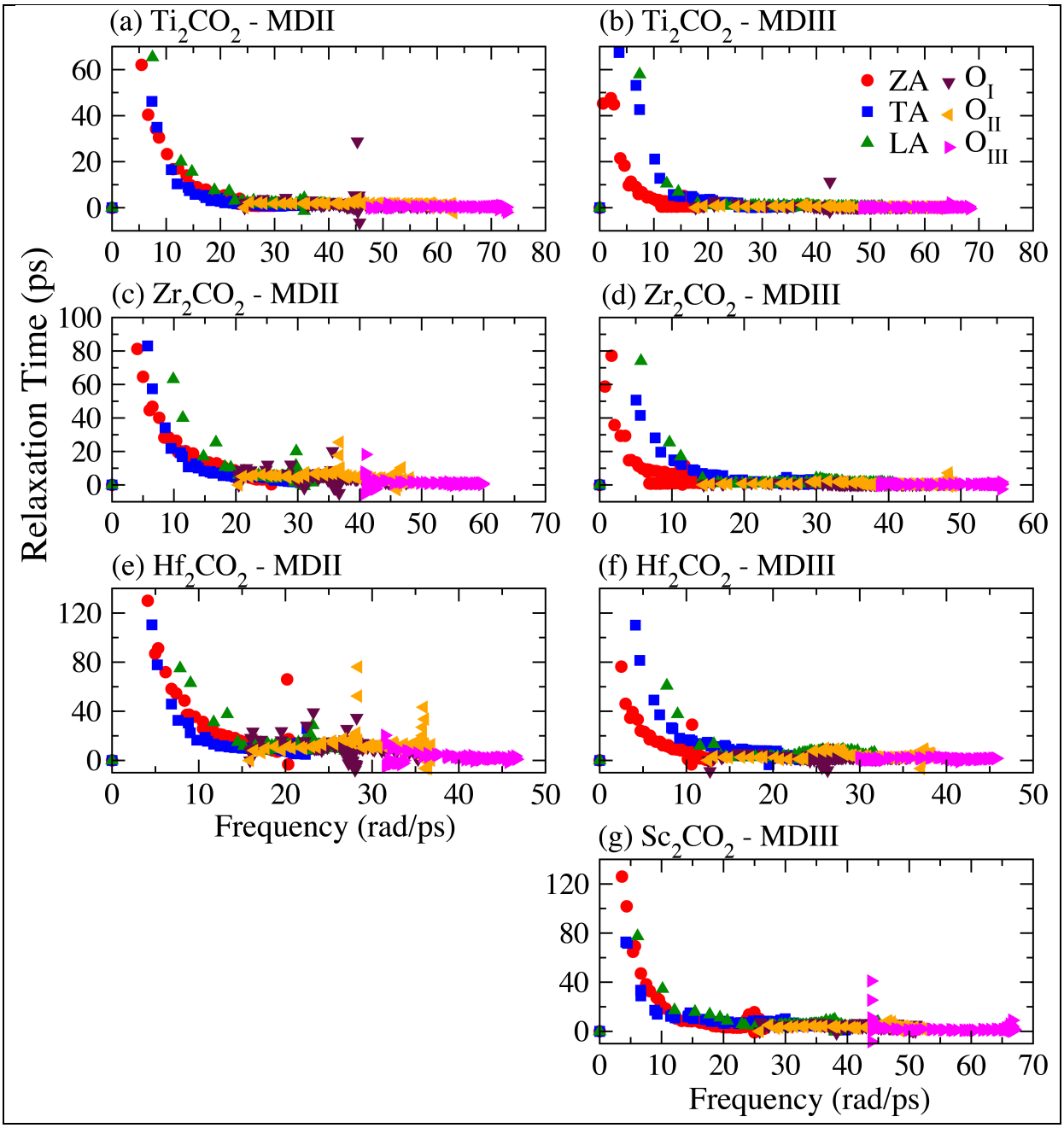

Figure S12: The dependence of relaxation time to frequency.

Since the calculated group velocities only provide a limited insight, we also calculated the relaxation time to have a better understanding of thermal conductivities. The TC is also affected significantly by relaxation time. Different phonon relaxation times between different materials are one of the main reasons that lead to a difference in the lattice TC. The frequency dependence of relaxation time of acoustic (LA-TA and ZA) and three lowest optical modes are demonstrated in Figure S12 for all the MXene structures considered in this study. The

acoustic branches have much higher relaxation times than optical branches. The relaxation times of optical branches represent weak frequency dependence whereas the phonon relaxation times of acoustic modes decrease as the frequency increases and exhibit frequency dependence as ω^{-2} at low frequency region. This dependency of the phonon relaxation time on the frequency is consistent with Klemens' prediction. According to our phonon calculations, the ZA branch is softer in MD-III than in MD-II. Thus, the relaxation time of this mode in MD-III is quite short as compared to that in MD-II. This translates into a lower TC in the former.

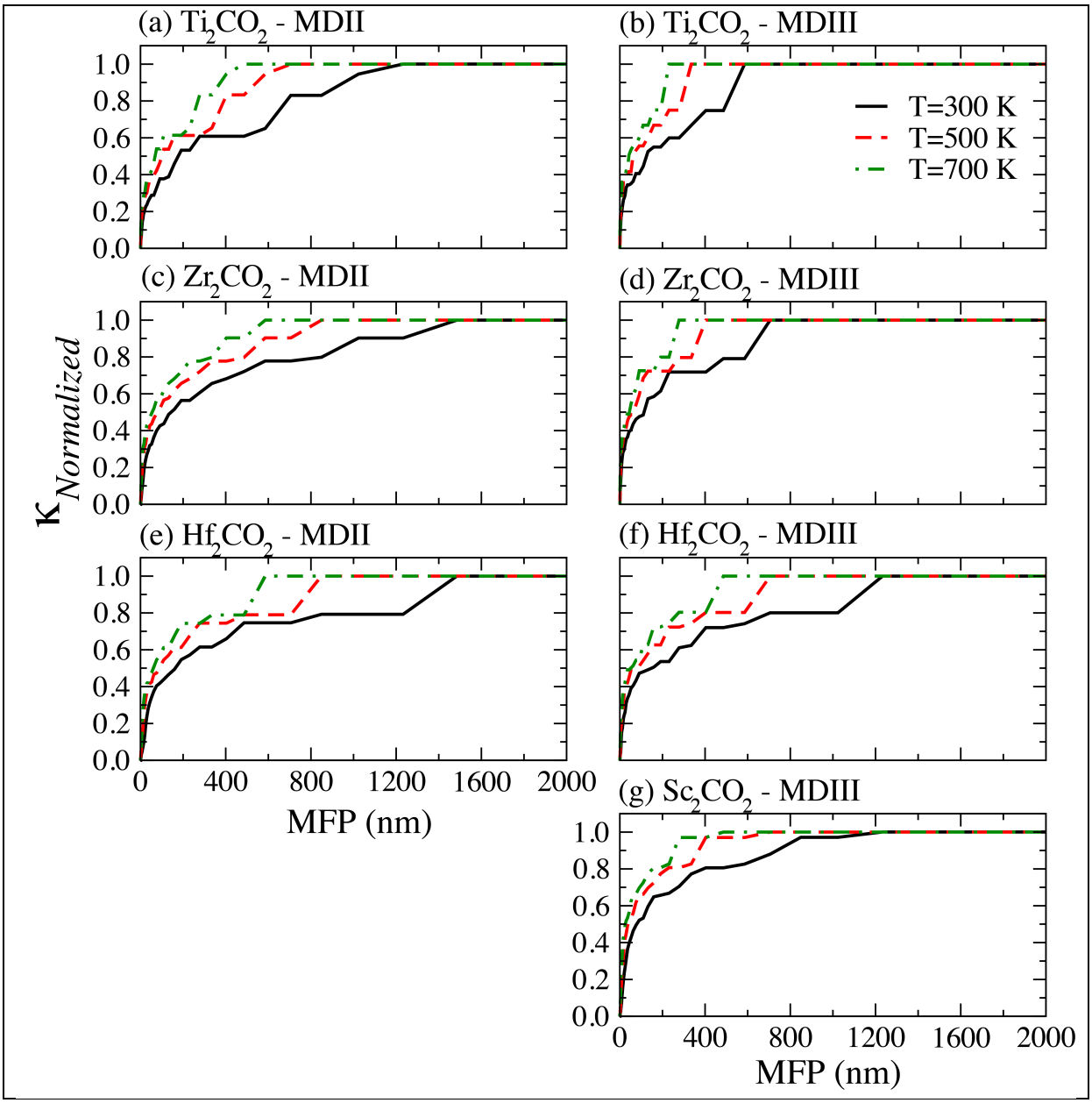

Figure S13: Lattice TC as a function of Mean Free Path at T = 300 K, 500 K and 700 K.

The phonon Mean Free Path (MFP) provides information about the average distance travelled by a phonon between scattering events and also it helps to understand the thermal conduction process in the related system. Figure S13 illustrates the dependence of normalized lattice TC on the MFP at different temperatures, namely T = 300 K, 500 K and 700 K. The contribution to lattice TC increases with increasing MFP value and then saturates after a certain value of MFP for each MXene structures. On the other hand, the lattice TC has its maximum value at

lower MFP values as the temperature increases. For all temperature values, Ti_2CO_2 in MD-III configuration has the lowest MFP at which the TC reaches its maximum value (585 nm at T = 300 K, 335 nm at T = 500 K and ~230 nm at T = 700 K). This means that; increasing temperature shortens the MFP and only phonons with MFP smaller than these values provides contribution to the lattice TC at related temperatures. Hence, the TC will have minimal contribution when the sample size is more than these MFP values. At T = 300 K, MD-II structures have maximum MFP values higher than 1.2 μm (~1.23 μm for Ti_2CO_2, ~1.48 μm for Zr_2CO_2 and Hf_2CO_2). This indicates that the heat is mostly transported by phonons with MFP in a wide range. Additionally, we listed the MFP values that corresponding to 50% contribution to normalized lattice TC for studied M_2CO_2 (M=Ti, Zr, Hf, Sc) materials at considered temperatures in Table I. This implies that; if the sample size becomes smaller than these MFP values, that effectively leads to a decrease in the lattice TC. Increasing temperature causes a reduction in the MFP. The lattice TC of the MD-III structure is saturated by phonons with much shorter MFPs as compared to the MD-II structure. For instance, in the MD-II configuration of Ti_2CO_2, the phonons with MFP shorter than 175 nm provide 50% of lattice TC, while the maximum MFP for MD-III configuration of Ti_2CO_2 to achieve a 50% contribution is only 120 nm. This means that TC is more ballistic (diffusive) in MD-II (MD-III) than MD-III (MD-II). Figure S13 also suggests that we may use much smaller sample sizes for the MD-III structure to achieve a maximum TC.

Table SI: The MFP value corresponding to 50% contribution to normalized lattice TC for MD-II and MD-III configurations of M_2CO_2 (M=Ti, Zr, Hf, Sc) at T = 300 K, 500 K and 700 K.

	T=300 K		T=500 K		T=700 K	
MFP(nm)	MD-II	MD-III	MD-II	MD-III	MD-II	MD-III
Ti_2CO_2	175	120	100	60	70	40
Zr_2CO_2	145	115	85	70	55	45
Hf_2CO_2	160	135	90	70	60	50
Sc_2CO_2	(Metal)	75	(Metal)	40	(Metal)	25